

Nanostructured Core-shell Materials based on Manganese Cobalt Oxide
and Nickel Molybdenum Oxide for Asymmetric Supercapacitor
Applications



Jaafar Mehrez
Advisor: Prof. Mai Liqiang

School of Materials Science and Engineering
Wuhan University of Technology

A Thesis Submitted for
MASTER'S DEGREE IN ENGINEERING
Wuhan, 430070, Hubei, P.R. China
2019

CONTENTS

Declaration	4
Abstract	5
Chapter I: Introduction	6
A. Supercapacitors in brief	7
B. Types of Supercapacitors	8
1. Electric double layer capacitors (EDLCs)	8
2. EDLC electrode materials	8
3. Pseudocapacitors	10
4. Mechanisms of Pesudocapacitance	10
5. Pseudocapacitive Materials	11
C. Nanoscale within Supercapacitor Electrode Materials	12
D. Research Objectives and Motivation	13
1. Contents of Thesis	13
Chapter II: Structural and Electrochemical Characterization Techniques	14
2. Hydrothermal Synthesis Method	14
3. Materials	15
4. Synthesis Equipment and Instrumentation	15
E. Experimental Procedure	15
1. Synthesis Method of MnCo ₂ O ₄ Nanowires	15
2. Synthesis of heterostructure MnCo ₂ O ₄ @NiMoO ₄ core-shell nanowire arrays	15
F. Physical Characterizations	16
1. X-Ray Diffraction (XRD)	16
2. Scanning Electron Microscopy (SEM)	16
3. Transmission Electron Microscopy (TEM)	17
4. X-Ray Photoelectron Spectroscopy (XPS)	17
5. Nitrogen Adsorption–Desorption Isotherm Technique	18
G. Electrochemical Characterization	18
1. Cyclic Voltammetry (CV)	19
2. Galvanostatic Charge and Discharge (GCD)	19
3. Electrochemical Impedance Spectroscopy (EIS)	19
Chapter III: One-dimensional MnCo ₂ O ₄ Nanowire Arrays for Supercapacitor Applications	20
H. Experimental Procedure	21
1. Synthesis of MnCo ₂ O ₄ Hetero-Nanostructures	21
2. Characterization	21
3. Electrochemical Measurements	21
I. MnCo ₂ O ₄ Nanowire Arrays (NWAs)	22
1. XRD and XPS Characterization of MnCo ₂ O ₄	22
2. Growth Mechanism of MnCo ₂ O ₄ NWAs	22
3. Morphology Characterization of MnCo ₂ O ₄ NWAs	23
4. Electrochemical Characterization of MnCo ₂ O ₄ NWAs	24
J. Chapter Summary	24
Chapter IV: Hierarchical MnCo ₂ O ₄ @NiMoO ₄ Core-Shell Nanowire Arrays with Synergistic Effect for Enhanced Supercapacitor Performance	25
K. Experimental Procedure	26
1. Synthesis of MnCo ₂ O ₄ Hetero-Nanostructures	26
2. Synthesis of MnCo ₂ O ₄ @NiMoO ₄ Core-Shell Hybrid Arrays	26
3. Fabrication of an Asymmetric Supercapacitor Device	26
L. MnCo ₂ O ₄ @NiMoO ₄ Hybrid Nanowire Arrays (NWAs)	27
1. XRD and XPS Characterization of MnCo ₂ O ₄ @NiMoO ₄ NWAs	27
2. Growth Mechanism of MnCo ₂ O ₄ @NiMoO ₄ NWAs	28
3. Morphology Characterization of MnCo ₂ O ₄ @NiMoO ₄ NWAs	28

4. Electrochemical Characterization of MnCo ₂ O ₄ @NiMoO ₄ NWAs	29
5. Electrochemical Characterization of pristine-NiMoO ₄ Nanosheets	31
6. MnCo ₂ O ₄ @NiMoO ₄ //AC Asymmetric Supercapacitor	32
M. Chapter Summary	33
Chapter V: Conclusion and Prospective of Future Work	33
N. Future Perspectives	33
References	34
Acknowledgements	38
Publications	39

Declaration

I declare that the thesis submitted is the research work and research results obtained by me under the guidance of my supervisor. To the best of my knowledge, except where specifically noted and acknowledged in the text, the thesis does not contain research results that have been published or written by others, nor does it contain research results that have been used to obtain a degree or certificate from Wuhan University of Technology or other educational institutions. Any contributions made by the people who work with me to this research have been clearly stated in the thesis and thanked.

Abstract

Electrochemical energy storage devices with emphasis on rational design at the material and device level are paving the way towards finding a worldwide solution to the global energy challenge as they provide an effective implementation of the electricity generated from renewable energy sources. Among the different energy storage devices, supercapacitors are well noted for their ultrafast charge and discharge ability, long operating life, and high power density ($1\text{--}10 \text{ KW}\cdot\text{kg}^{-1}$). However, supercapacitors still face the problem of low energy density. In order to increase the energy density, tremendous research efforts have recently been made to enhance the specific capacitance and working voltage window. One of the approaches towards achieving higher specific capacitance is the implementation of pseudocapacitive electrode materials, which are mainly composed of transition metal oxides and conducting polymers that store charges faradaically at the surface/near surface, resulting in high capacitance and energy density. On the other hand, a wider potential window will be realized when implying an asymmetric cell configuration, combining two different materials with different capacitive mechanisms.

Owing to the high capacitance of pseudocapacitive electrodes, transition metal oxides have been well studied and exploited to enhance the energy densities of supercapacitors. Nevertheless, the practical implementation of metal oxide based materials as supercapacitor electrodes still suffer from moderate electronic conductivity and relatively low specific capacitance. The unique synergistic effect of hierarchical core-shell structures demonstrates great potential for designing the next-generation electrode materials for supercapacitors. In this thesis, manganese cobalt oxide and nickel molybdate oxide were studied as electrode materials for supercapacitors. The MnCo_2O_4 nanowire arrays (NWAs) were firstly grown directly over a nickel foam substrate without any binders, and then characterized as a cathode material for supercapacitors. Subsequently, NiMoO_4 nanosheets were grown and coated over the previous MnCo_2O_4 nanowire arrays, resulting in a unique hybrid Core-Shell structure. The as-prepared electrodes were studied and characterized individually before fabricating a full asymmetric supercapacitor device. The main results are the following:

1. Simple and facile hydrothermal method combined with post-annealing was introduced to controllably design MnCo_2O_4 nanowire arrays over a substrate of nickel foam without using any binders. The sample was characterized by TG, XRD, XPS, SEM and TEM and then carefully tested as cathode for supercapacitors.
2. The electrochemical performance of the manganese cobalt nanowire hybrid arrays was tested and it displays a specific capacitance of $457.58 \text{ F}\cdot\text{g}^{-1}$ and a 74% rate capability between $1\text{--}10 \text{ A}\cdot\text{g}^{-1}$ capacitance range and a high capacitance retention of 100% after 10000 cycles at $5 \text{ A}\cdot\text{g}^{-1}$.
3. Using a second hydrothermal process with post-annealing, the previous manganese cobalt nanowires were coated with a layer of nickel molybdate nanosheets. The sample was characterized by XRD, XPS, SEM, TEM and BET to confirm the chemical composition and crystal structure. After that, the $\text{MnCo}_2\text{O}_4@\text{NiMoO}_4$ core-shell were tested as a cathode for supercapacitors.
4. The electrochemical performance of the $\text{MnCo}_2\text{O}_4@\text{NiMoO}_4$ core-shell NWAs was tested displaying great improvements, such as a high specific capacitance of $1244 \text{ F}\cdot\text{g}^{-1}$ and a 91% rate capability between $1\text{--}10 \text{ A}\cdot\text{g}^{-1}$ capacitance range and a capacitance retention of 85% after 2500 cycles upon $5 \text{ A}\cdot\text{g}^{-1}$.
5. For further comparison, NiMoO_4 nanosheets were grown directly over nickel foam substrate. The electrochemical performance of the pure- NiMoO_4 was $762.5 \text{ F}\cdot\text{g}^{-1}$ and a 64% of rate capability between $1\text{--}10 \text{ A}\cdot\text{g}^{-1}$ capacitance range and a capacitance retention of 73% after 2500 cycles upon $5 \text{ A}\cdot\text{g}^{-1}$.
6. Using the $\text{MnCo}_2\text{O}_4@\text{NiMoO}_4$ core-shell NWAs as a cathode and commercially available active carbon (AC) as an anode, we assembled and tested an asymmetric supercapacitor (ASC). The device displayed high energy density of $42 \text{ W}\cdot\text{h}\cdot\text{kg}^{-1}$ at a power density of $852.3 \text{ W}\cdot\text{kg}^{-1}$ and a good cyclability with 93% of the initial capacitance retained at the end of 8000 successive charge/discharge cycles.

For this consideration and building upon the study within this thesis, the $\text{MnCo}_2\text{O}_4@\text{NiMoO}_4$ core-shell NWAs electrode material holds a great promise for manifesting reliable energy storage devices.

Chapter I: Introduction

Energy has always been related to prosperity of human lives. Physically, energy is a quantitative property that must be transferred to an object to perform work. It is a conversed quantity according to the law of conservation of energy, which states that energy can be converted in form, but not created or destroyed. The most common forms of energy include the kinetic energy of a moving object, the potential energy stored by an object's position in a force field, the elastic energy, the chemical energy released out of a chemical reaction, the radiant energy carried by light and the thermal energy due to an object's temperature. There is an increasingly diverse array of energy sources, which could be categorized in two broad fields. Firstly, the non-renewable energy, it is an energy source that diminish over time, and those sources are not able to replenish themselves. For that, they are finite, and once they are used, they are effectively gone because they take so long to reform. For example, fossil fuels like coal, oil, and natural gas are all examples of fossil fuels, which get their energy from the sun, but none of them is renewable. They all emit CO₂ when burned causing harm and environmental pollution. Nuclear energy is also a non-renewable energy source. Even though, it is a carbon-free source and for that, it is not a fossil fuel, but it results in radioactive waste. On the other hand, renewable energy is a resource that rely on fuel sources that restore themselves over short periods and do not diminish, and have various benefits and drawbacks. For example, solar, wind and hydraulic are renewable and carbon-free, and effectively inexhaustible. The production of renewable energy is largely variable and difficult to control.

In contrast to fossil energy, renewable energy must therefore be harvested when it is available, and to maintain the balance between production and consumption, some sort of energy storage is needed or at least of value. At present, the balance between consumption and production is relatively easy to maintain, since most of the energy we consume is stored in fossil fuels, which can be readily used when needed. However, as the penetration of renewable energy increases, balancing production and consumption will become more challenging. The biggest challenges are in the electricity sector, where the real-time balance between production and consumption is closely linked to grid stability. For that, we focus on energy storage technologies and their possible uses in our daily life. Because many electronic devices (such as laptops, smartphones and vehicles) have become an integral part of an increasingly more mobile man. There is a pressing need to find economical, long-lasting and ecologically friendly ways to store the energy we harness from diverse sources. energy storage systems (ESS) including lithium-ion batteries and supercapacitors (electrochemical capacitors or ultracapacitors) as electrochemical energy storage systems are widely used for powering the now-ubiquitous portable electronics in our society and

for the electrification of the transportation sector because of the high energy density of lithium-ion batteries and high power density of supercapacitors. In particular, supercapacitors have been developed and proposed to address some of those energy storage needs because of their unique advantages on rapid charge/discharge and long cycle life.

Supercapacitors are rechargeable electrochemical energy storage devices that offer a high power density, and longer cycling lifetime compared with traditional batteries, but still lack the efficient energy density. According to the application, supercapacitors can replace or complement batteries where high power is required, ranging from electrical engines for vehicles to power-pulse applications. Depending on the storage mechanism and cell configuration, supercapacitors can be divided in three types. Electric double-layer capacitors (EDLCs), pseudocapacitors, and hybrid capacitors. EDLCs are based on high specific-surface area nanoporous materials ($> 1000 \text{ m}^2 \cdot \text{g}^{-1}$) as active electrode materials, leading to a huge capacitance in comparison with electrostatic capacitors. The charge storage mechanism is based upon physical adsorption at the electrode/electrolyte interface. Nanoporous carbon materials are usually used as EDLCs electrodes thanks to their availability, existing industrial production and low cost. On the other hand, pseudocapacitors composed mainly of transition metal oxides and conducting polymers store charges faradaically at the surface/near surface but not in the bulk like batteries, resulting in high capacitance and energy densities compared with carbon-based EDLCs. However, like in the case of batteries, redox reactions can lead to mechanical changes causing the electrodes to swell and shrink, giving rise to poor mechanical stability. Finally, hybrid capacitors are composed of an EDLC electrode and a pseudocapacitive or battery type electrode, combining the properties of both systems and leading to an intermediate performance.

One of the main challenges for pseudocapacitors is the relatively low electrical conductivity, which results in relatively lower rate capabilities.[1] A problem that could be approached by implying smart nanostructure designs. Such nanostructured materials can increase the active surface area; shorten the electron and ion transport pathways, reduce the diffusion resistance for electrolytes and effectively accommodate the structural change or strain.[2] Electrochemical performance could also be improved by combining different electrode materials in various architectures resulting in the increase of ion diffusion kinetic and electron transport at the electrode/electrolyte interface. In this study, we aim to apply the theoretical concepts of nanostructures within supercapacitor electrode materials and systematically test the pseudocapacitive behavior of the prepared materials. We further aim to contribute to the development of novel fabrication routes for the formation of supercapacitor electrodes with enhanced characteristics.

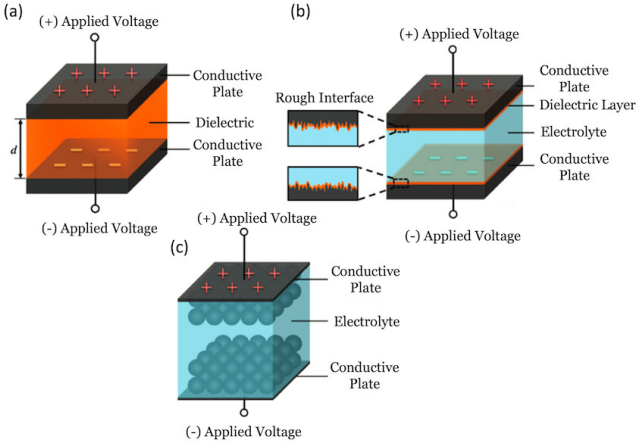


Figure 1. (a) Dielectric capacitor, (b) Electrolytic capacitor, and (c) Electrochemical capacitor (supercapacitor).

A. Supercapacitors in brief

A capacitor is a high-power storage device, which stores charges on the surface of its electrodes.[3] The key performance characteristic of such device is the capacitance, which is defined as the ratio of the charge accommodated by one of the two electrodes divided by the voltage applied across the device that induces this charge [Eq. 1].

$$C = \frac{S}{d} \quad (1)$$

Where C is the capacitance, S is the electrode surface area, d is the charge separation distance and ε is the absolute permittivity, which is a product of relative permittivity ε_r of the dielectric (charge separation layer) and the permittivity of vacuum ε_0 . According to [Eq. 1], the capacitance is proportional to the electrode surface area and absolute permittivity, while it is inversely proportional to the charge separation distance. The oldest type of capacitors is dielectric capacitor, consisting of two parallel conductors separated by a dielectric layer as shown in [Fig. 1 (a)]. The basic features of such type of capacitors is being limited in capacitance, but having a very fast response to external applied voltage. The applications of dielectric capacitors differ according to their size, smaller versions of these devices are used in various electronic equipment like current controls and electric filters, while larger dielectric capacitors are used as ultrahigh-power and high voltage energy storage devices. The other type of capacitors is electrolytic capacitors [Fig. 1 (b)]. As we can see, the space between the two electrodes is filled with ionically conductive liquid or solid electrolyte, both the anode and the cathode have high surface area and are porous in nature. Compared with dielectric capacitors, electrolytic capacitors offer higher capacitance due to larger surface area and thinner charge separating dielectric layer. The last type in the field of capacitors is

electrochemical capacitors (EC) [Fig. 1 (c)]. They are often called supercapacitors which possess relatively higher capacitance compared to the other two types. Supercapacitors can be divided into three categories according to charge storage mechanism: (1) electric double-layer capacitors (EDLC), (2) pseudocapacitors, and (3) hybrid capacitors.

The Ragone plot in [Fig. 2] shows that supercapacitors fill in a critical position between conventional capacitors and batteries in terms of both energy and power density. The specific energy axis represents how much energy a device can store, while the specific power density axis represents how rapidly this energy can be delivered from/to the device, which is related to how fast this device can be charged and discharged.[4] Comparing supercapacitors with lithium-ion batteries (LIBs), which possess a higher energy density than supercapacitors.[5] However, suercapacitors can be charged/discharged in mere seconds as opposed to hours for batteries.[6] For that, a higher power density could be revealed by supercapacitors ($1\text{-}10 \text{ kW}\cdot\text{kg}^{-1}$),[7] as well as the longer cycling life ($50,000\text{--}2,000,000$ cycles).[6] Building upon previous features, supercapacitors have been proposed as an alternative to batteries, where they could be used on their own as an efficient and long-lasting energy storage device, or coupled with a battery. Table I contains a comparison of some important characteristics of state-of-the-art electrochemical capacitors and lithium-ion batteries.

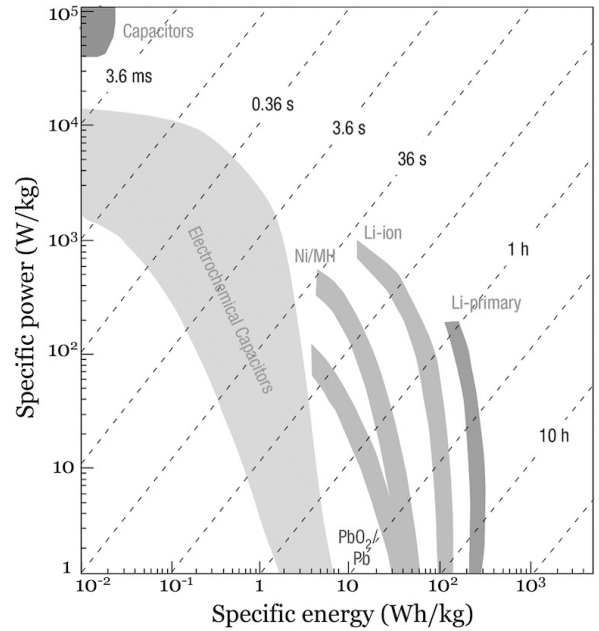


Figure 2. Ragone plot showing the location of different energy storage devices according to their capabilities.

Table I. Comparison of some important characteristics of state-of-the-art electrochemical capacitors and lithium-ion batteries.

Characteristic	State-of-Art Lithium-ion Batteries	Electrochemical Capacitors
Charge time	~ 3-5 min	~ 1 s
Discharge time	~ 3-5 min	~ 1 s
Cycle life	< 5,000 @ 1C rate	> 500,000
Specific energy (Wh/kg)	70-100	5
Specific power (kW/kg)	0.5-1	5-10
Cycle efficiency (%) (kW/kg)	< 50% to > 90%	< 75% to > 95%
Cost/Wh	\$1-2/Wh	\$10-20/Wh
Cost/kW	\$75-150/kW	\$25-50/kW

B. Types of Supercapacitors

Supercapacitors can fall into three categories depending on charge storage mechanism or cell configuration: (1) Electric double layer capacitors (EDLCs), (2) pseudocapacitors (also known as redox supercapacitors) and (3) Hybrid supercapacitors.[7] The basic difference between pseudocapacitors and EDLCs is in the way charge is being stored at the capacitor. For EDLCs, the charge separation takes place across the electrical double layer defined by the charged surface of the electrode and the absorbed electrolyte ions of the opposite sign, while for pseudocapacitors, the charge storage occurs as a result of rapid Faradic redox reactions occurring at/near the electrode surface.[8]

1. Electric double layer capacitors (EDLCs)

In order to understand the charge storage mechanism within EDLCs, we need to explain the phenomena of electric double layer, which is a structure layer that appears when a charged object is placed into a liquid. The balancing counter charge for this charged surface will form on the liquid, concentrating near the surface.[7] The proposed models for this phenomenon are shown in [Fig. 3], within those three illustrated models Ψ is the potential, Ψ_0 is the electrode potential, IHP is the inner Helmholtz plane, and OHP is the outer Helmholtz plane. The first and simplest approximation was Helmholtz model [Fig. 3 (a)], which considers the existence of rigid layers counterbalancing the charges from the solid at a distance d from that solid electronic conductor.[9] The other suggested model is Gouy-Chapman model [Fig. 3 (b)], also known as the diffuse model. In this model, the ions are not rigidly attached to the surface as in Helmholtz model, and those ions in the solution tend to diffuse into the liquid phase until the counter potential set up by their departure restricts this tendency. The last proposed model is Stern model or the diffuse double layer model [Fig. 3 (c)]. In this model, Stern resolved the shortcomings of the Gouy-Chapman model for the diffuse layer, suggesting the combination of both previous models, giving an internal Stern layer and an outer diffuse layer.[10]

The above-mentioned models are suitable to describe

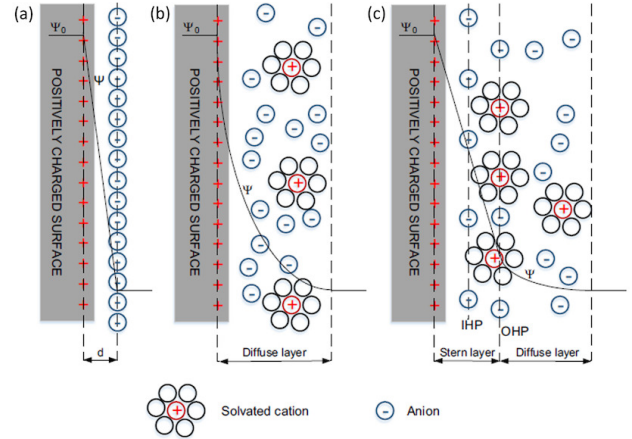


Figure 3. EDL models, (a) Helmholtz model, (b) Gouy-Chapman model, (c) Stern model

the EDL in plane surfaces, but for the nanoporous materials used in supercapacitors, they fail in describing the real situation. The mobility of ions into the pores of electrode material is greatly influenced by the pore size, and ions do not move into the bulk of electrolyte the same way they move within the pores. Consequently, if the pore size is inaccessible to the ions, it is not going to contribute to the double layer capacitance.[11] And since not all the pores are accessible to the ions, there is no linear relation between the capacitance exhibited by the material and its specific surface area.[12][13][14][15]

2. EDLC electrode materials

Carbon materials are found to be suitable materials for supercapacitor electrodes due to their large reservation in nature, low cost, environmental benignity, facile processing procedure, controllable pore size, high specific surface area, high electric conductivity, good chemical stability and stable performance in wide range of temperatures. Carbon materials are basically utilized in electric double layer capacitors due to stability of carbon materials in the electrolyte. These materials show a nearly rectangular shape cyclic voltammogram [Fig. 4(a)] with no redox peaks, and the charge-discharge curves in [Fig. 4(b)] are

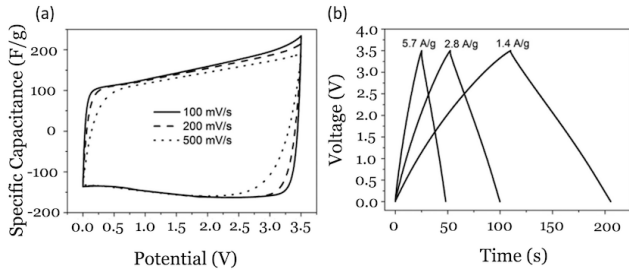


Figure 4. (a) Cyclic voltammetry curves of microwave exfoliation/reduction of GO electrode at different scan rates, (b) Galvanostatic charge-discharge curves of microwave exfoliation/reduction of GO electrode under different current density.[16]

basically symmetrical, indicating high columbic utility ratio of electrostatic energy storage method. Since carbon materials are only able to store electrical energy on the surface of the electrode, the capacitance of carbon materials is mainly associated with the characteristics of electrode surface such as specific surface area, pore volume, pore shape, pore size distribution, and conductivity. Currently, many carbon materials with high specific surface area have been reported such (AC),[17–21] carbon nanotubes (CNTs),[22–24] and graphene.[25–27]

1. Activated Carbon: Highly porous activated carbons (ACs) have become the most widely used materials in commercial EDLCs. This is because of their high SSA, high chemical stability, reasonable cost, tunable properties, abundance and diversity of precursors. ACs could be produced in various shapes and forms using a combination of thermal treatments and partial oxidation of organic compounds. General methods for preparing ACs could be classified into two categories: Physical (or thermal) activation and chemical activation.[28] The former method may contain two steps: Firstly, carbonization of a precursor or the removal of the majority of noncarbon species by thermal decomposition in inert or partially inert atmosphere and gasification, which is used to enhance the porosity by partial etching of carbon during the heat treatment in the presence of an oxidizing agent.[29] On the other hand, chemical activation is often conducted in one-step, by mixing the precursor with an activation agent and heating. In this case, pore formation and removal of the noncarbon species proceed simultaneously. The drawback of this method is that it requires extensive post-activation cleaning, which increases the production cost. Compared to physical activation, chemical activation generally results in larger volume of micropores, higher carbon yield, and more uniform pore size distribution.[30] It is reported that an activated carbon-based supercapacitor with up to $3000 \text{ m}^2/\text{g}$ specific surface area only has the specific capaci-

tance less than $10 \mu\text{F}/\text{cm}^2$, which is smaller than theoretical capacitance. Thus, the utility ratio of high specific surface area is also essential to the behavior of supercapacitors.[31] To increase the efficiency of surface area, it is necessary to adjust the pore shape, pore size distribution, and the pore volume. Generally, the capacitance of AC in aqueous electrolyte is from 100 to 300 F/g.[32]

2. Carbon Nanotubes (CNTs): Carbon nanotubes could be categorized according to the direction of rolling a graphene sheet into zig-zag, armchair, and chiral CNTs as shown in [Fig. 5]. This type of carbon materials is well known for their high conductivity, good mechanical stability, benign chemical and thermal properties, as well as the unique porosity. Owing to their high conductivity, CNTs are preferred electrode materials for high power density devices. The low resistance value can lead to high power density. Besides, the low resistance of CNTs also leads to a better rate capability. It is been reported that CNTs could be combined with faradic materials, in which high power density is achieved by CNTs and the high energy density comes from the faradic materials. For example, MnO_2 ,[33] and V_2O_5 .[34]
3. Graphene: Graphene was firstly discovered during the study of graphite in Manchester University in 2004 by Geim and his colleagues.[35] Graphene could be regarded as a single layer of graphite and it is a two-dimensional (2D) carbon sheet forming by sp^2 -hybridized. It has a special honeycomb structure, which is possible to be built into many other allotropes of carbon such as CNTs, graphite, and fullerenes. Each single layer of graphene is composed of hexagonal sp^2 carbon atoms. This specific structure possesses some unique features like high mechanical stability, thermal stability, and special electrical property. The extraordinary high surface area of graphene ($2675 \text{ m}^2/\text{g}$) makes it a good choice for the high performance of electric double layer capacitors. In that case, if the high specific surface area was fully utilized, then the specific capacitance of EDLCs could reach 550 F/g.

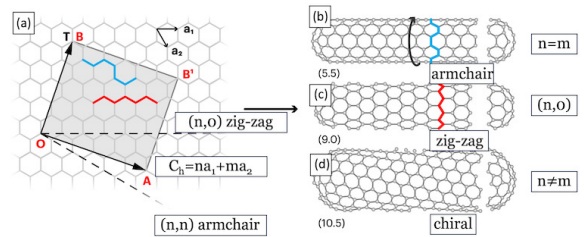


Figure 5. (a) Different atomic structures corresponding to the direction of rolling a graphene sheet, (b) atomic structure of zig-zag, (c) atomic structure of chiral CNTs, (d) atomic structure of armchair CNTs.

Many studies of graphene-based electrode materials for supercapacitors have been reported in different electrolytes, like aqueous and organic electrolytes. The most famous synthesis methods that have been adopted to prepare graphene-based supercapacitor electrode materials are chemical modification, microwave irradiation, thermal treatment of graphene oxide at high temperatures, and at low temperature but in vacuum. The achieved capacitance of aqueous supercapacitors with graphene-based electrodes is between 130 and 200 F/g,[36] and a lower capacitance for organic electrolytes from 100 to 150 F/g. As we can see, the specific capacitance of graphene-based electrodes in practical application is not able to reach the theoretical value, because graphene sheet has a high possibility of restacking during the preparation, leading to the lack of sufficient utilization of surface area in graphene. In order to solve the graphene restacking problem, composites made of graphene and metal oxides have been suggested. Such composites are beneficial for both materials, as metal oxides will prevent the graphene from agglomeration and restacking, and increase the available surface area. On the other hand, graphene will help metal oxides to form nanostructures with uniformly dispersed controlled morphologies.

3. Pseudocapacitors

In the face of the significant recent developments and commercial success, EDLCs still lack the high capacitance needed for high energy density, which is 20–200 times smaller than that of rechargeable Li-ion batteries. Therefore, materials that exhibit reversible redox reactions in the electrode potential window, such as transition metal oxides and conductive polymers, have been incorporated willing to boost the capacitance and energy density of supercapacitors. Pseudocapacitors store the electric charge *via* reduction and oxidation of electrolyte ions in reversible charge transfer reaction at the electrode. Compared with EDLC, which is free of charge transfer, the double layer pseudocapacitors have a net ion exchange between the electrode and electrolyte during the charge/discharge processes. This process is similar to the analogous process happening in batteries, except that in pseudocapacitors such processes are limited to the surface of active materials. The distinction between the pseudocapacitor electrodes and the high rate battery electrodes may become vague. [Fig. 6] shows the CV and charge/discharge curves of three types of electrochemical capacitor electrode materials. As we can see, EDLC electrode materials exhibit a flat CV curve with a semi-rectangular shape, and linear voltage responses during constant-current discharge. In other words, an EDLC material will show linear current response dependency on the scan rate ($i \sim v$). Compared with battery-like electrode materials, which exhibits a sharp peak in CVs

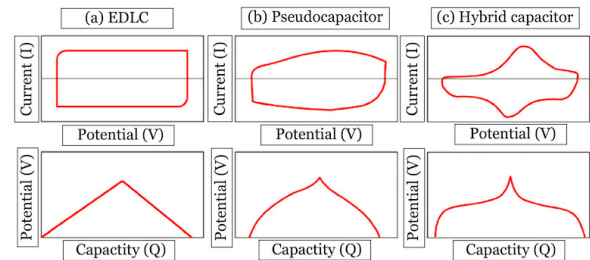


Figure 6. Typical CV (upper) and charge-discharge (lower) curves of three types of electrochemical capacitors: (a) EDLC, (b) Pseudocapacitors, and (c) Hybrid capacitors.

and characteristics plateaus in the charge/discharge due to the phase transformations taking place during the redox reactions. While pseudocapacitors lies in between, with very broad redox peaks in CV.

4. Mechanisms of Pseudocapacitance

Several faradic mechanisms have been identified by Conway that can result in capacitive electrochemical features: (1) Underpotential deposition, (2) redox pseudocapacitance and (3) intercalation pseudocapacitance. The underpotential deposition occurs when metal ions form an adsorbed monolayer at a different metal's surface well above their redox potential. While redox pseudocapacitance occurs when ions are electrochemically adsorbed onto the surface or near surface of a material with faradic charge-transfer. The last mechanism of intercalation pseudocapacitance occurs when ions intercalate into the tunnels or layers of a redox-active material with faradic charge-transfer and no crystallographic phase change. The similarity in the electrochemical signatures of those mechanisms occurs due to the relationship between potential and the extent of charge that develops because of adsorption/desorption processes at the electrode/electrolyte interface. [Fig. 7] shows the different mechanisms of pseudocapacitance.

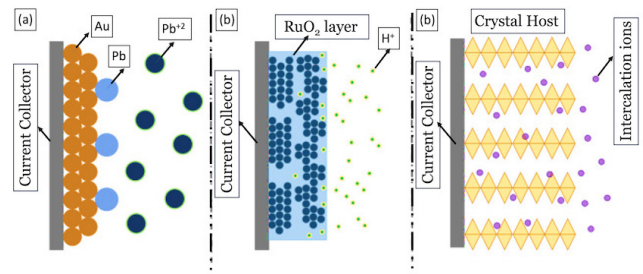


Figure 7. Reversible redox mechanisms that give rise to pseudocapacitance: (a) Underpotential deposition, (b) Redox pseudocapacitance, and (c) Intercalation pseudocapacitance.

5. Pseudocapacitive Materials

Contrasted to carbon materials, which store charges in the electric double layer, pseudocapacitive materials with fast redox reactions on or near the surface of the electrode are capable to achieve higher specific capacitances in the order of 10–100 times higher than carbon materials. Pseudocapacitive materials are widely studied in recent years in order to develop advanced electrode materials for the next generation of supercapacitors. Generally, pseudocapacitive materials can be divided into two categories: Conductive polymers and transition metal oxides.

1. Conductive polymers: Conducting polymers are rendered conductive through a conjugated bond system along the polymer backbone. They are typically formed through chemical oxidation of the monomer or electrochemical oxidation of the monomer.[37] Conductive polymers are generally low-cost, environmentally friendly, and their source is extensive. Besides, conductive polymers have high conductivity, wide potential window and high porosity, making them promising candidates for supercapacitor electrode materials. Conductive polymers only have conductive property at a doped state, which is mainly because conductive polymers are positively or negatively charged by oxidation or reduction processes. During charge and discharge process, redox reactions occur on the surface and in the bulk near the surface of the conductive material. The ions attracted from the electrolyte to the polymers during the oxidation reaction and then released back during reduction. Since there is no phase change during those redox reactions, conductive polymers competent for long life cycling. The most commonly used conductive polymers for supercapacitor applications are: Polyaniline (PANI),[38] polypyrrole (PPy),[39] poly(3,4-ethylenedioxythiophene) (PEDOT),[40] and polythiophene (PTh).[41] It should be noted that conductive polymers can work well only under certain conditions, like using electrolyte and right potential window, because under improper operating voltage window, conductive polymers may lose conductivity or be degraded.[42]
2. Transition metal oxides: Compared with polymers, transition metal oxides (TMOs) are able to possess higher specific capacitance and better cycling stability as faradic materials. The higher specific capacitance is coming from the fact that TMOs have two or more oxidation states in the same phases. For that, when charge and discharge take place, TMOs are able to convert between different oxidation states, while protons are able to insert into and extract from the oxide lattice during reduction and oxidation. Those reduction reactions are fast and reversible, since no phase change occurs in the process. TMOs were widely studied as supercapacitor electrode materials and were found to have the previous properties, such as RuO₂,[43] MnO₂,[44] and Co₃O₄.[45] As an example, hydrated ruthenium oxide (RuO₂.nH₂O) is one of the most popular pseudocapacitor electrode materials, that has been widely studied because of its high conductivity and the three accessible distinct oxidation states within a potential window of 1.2 V.[46] In aqueous acidic solutions, the pseudocapacitance of (RuO₂.nH₂O) is achieved by fast, reversible electron transfer and with electroadsoption of protons on the surface of (RuO₂.nH₂O) particles. Capacitance of more than 600 F.g⁻¹ has been achieved by (RuO₂.nH₂O).[47] However, the high cost of (RuO₂.nH₂O) hindered its application for mass production, which paved the way to seek less expensive oxides with similar properties. Among those oxides, MnO₂ was found to be a promising candidate, with a storage mechanism based upon surface adsorption of electrolyte cations and protons.[48]
3. Spinel structures of transition metal oxides: The spinel crystal structure, with a general formula of AB₂O₄, is holding a great promise for supercapacitor electrode materials, owing to the robust crystalline structure with three-dimensional (3D) diffusion pathways. Spinel structures are categorized into two types: (1) Single or mono spinel metal oxides, and (2) mixed or binary spinel metal oxides. For example, Mn₃O₄, Fe₃O₄ and Co₃O₄ as single spinel transition metal oxides exhibit the characteristics pseudocapacitive features with mostly rectangular CVs.[49] However, for Co₃O₄, the behavior is a little bit different.[50] Such spinel materials can exhibit a battery-type behavior due to the formation of oxyhydroxides during the charge storage process in an alkaline electrolyte, according to the following reaction:[51] $M_3O_4 + OH^- + H_2O \leftrightarrow 3 MOOH + e^-$ The two-phase reaction of previous equation involves one phase transformation, which results in a constant potential during galvanostatic charge-discharge, and limits the rate capability. However, when M = Co, the electrochemically formed oxyhydroxide get involved in a second reversible redox process: $CoOOH + OH^- \leftrightarrow CoO_2 + H_2O + e^-$ We could conclude that the electrochemical signature of such material includes pseudocapacitive and battery-like contributions. The same thing will be applied for mixed or binary spinel metal oxides, as an example spinel cobaltites (MCo₂O₄; M = Mn, Ni, Zn, Cu, etc.) have been documented to possess superior electrochemical performance to single or mono metal oxides,[52] which is a result of having higher electrical conductivity than simple spinel metal oxides owing to the relatively low activation energy for electron transfer between cations.[53] The preparation of those materials in nanoscale form is ex-

pected to emphasize the pseudocapacitive contribution.

C. Nanoscale within Supercapacitor Electrode Materials

One of the remarkable ways to improve the energy storage capabilities of supercapacitors is nanostructuring the electroactive electrode materials. Current research efforts are being devoted towards exploring the possibilities of using self-supported homogeneous and heterogeneous nanoelectrodes in the forms of one-dimensional (1D), 2D nanoarrays, and 3D nanoporous architectures. The energy density of a supercapacitor is proportional to the capacitance (C) and the voltage window (V) according to the following equation:

$$E = \frac{CV^2}{2} \quad (2)$$

In the above equation, it is clearly seen that in order to increase the energy density of supercapacitor cell, we can achieve that by increasing either or both capacitance and the cell potential. In the case of EDLC, the capacitance largely depends on the specific surface area of electrode material. Pseudocapacitive materials can also make benefit of the high surface area of electrode material, because it allows more materials availability for the interfacial Faradic reactions, and thus more charge will be stored, resulting in a higher energy density. The key point of using nanomaterials and nanostructures as electroactive materials is based upon the fact that nanomaterials have an extraordinary high surface area-to-volume ratio, making more electroactive materials accessible to

the electrolyte for the double-layer formation and/or reversible Faradic reactions.[55]

In general, nanostructured electroactive materials are synthesized in the form of either powder or freestanding arrays. The powdery form is preferred for its synthesis easiness in large scales, however, the use of binders and conductive additives to the powder form in order to cast supercapacitor electrodes will generate some dead volume in the fabricated electrodes, resulting in low utilization ratio of electroactive materials.[56] On the other hand, the binder-free electrodes are fabricated by the direct growth of electroactive materials over a conductive substrate, which is considered highly desirable method for fabricating supercapacitor electrodes without the need of any other additives. Compared with slurry-casting electrodes, binder-free electrodes show some unique features, such as improved utilization of electroactive materials and enhanced charge/ion transportation. Binder-free electrodes could be classified into two categories: (1) Homogeneous nanoelectrodes, which is made of a single electroactive material in the shape of nanoarrays, and (2) heterogeneous nanoelectrodes, that is nanoarrays consisting of either electroactive materials with nanostructured current collectors/supporters or more than one kind of electroactive materials in single nanoelectrodes. The most general form of heterogeneous nanoelectrodes is the core-shell architecture, in which a shell of electroactive material is conformably deposited over a core of free-standing nanostructured current collectors or another kind of electroactive material that are grown on a conductive substrate.[57]

The general way to fabricate self-supported nanoelectrodes is by synthesizing nanoarrays of electroactive materials on a conductive substrate. In specific, the 1D nanoarrays such as nanowires, nanorods, and nanotubes are considered to be suitable for supercapacitor application due to the fact that the longitude axis of 1D nanostructures could provide efficient transport pathways for both electrons and ions, leading to high charge/discharge rate.[58] For instance, Li *et al.* reported a 1D nanowire array in a spinel structure of binary metal oxide $MnCo_2O_4$ grown directly over a conductive substrate of nickel foam,[59] the as-synthesized material exhibits excellent properties for electrochemical energy storage with a high capacitance of 349.8 F.g^{-1} at 1 A.g^{-1} and a good rate capability. The outstanding performance is mainly attributed to the nanowire array architecture, which provides large reaction surface areas, fast ion and electron transfer and good structure stability. Another important geometry is the 2D nanoarrays, such as nanosheets, nanowalls, and nanoflakes. This structure can possess the mutual merits with 1D nanostructures as electrode materials for supercapacitors, such as large specific surface area, porous feature to increase the amount of electroactive sites, direct pathways for electron transport, and shortened pathways for ion diffusion.[60] The 2D nanoarrays could be grown directly over conductive substrates, for instance, free-standing 2D $NiCo_2O_4$

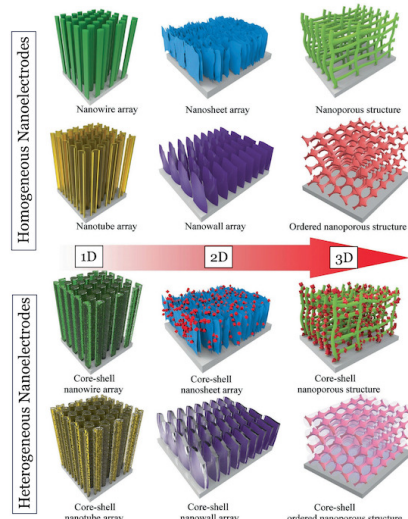


Figure 8. Schematic illustration of self-supported homogeneous and heterogeneous nanoelectrodes for supercapacitors.[54]

nanosheet arrays reported by Zhang *et al.* The mesoporous nanosheets have been prepared by a simple solution method with different substrates and delivered ultrahigh capacitance and excellent high-rate and cycling stability when tested as supercapacitor electrode materials.[61]

Those 2D architectures could also be deposited over a scaffold core material in a core-shell heterostructure design. In such way, the 1D nanostructure as a core will provide the efficient and stable pathways for electron transport and reduce the ion diffusion length, while 2D nanostructures can ensure more electroactive sites and higher accessible surface area for ions when used as a shell. Building upon those features of 1D and 2D nanostructures, the core-shell structure holds a promising role for providing the required fast ion-electron transport pathways as well as buffering the change in volume during charge-discharge processes. Many research groups have deployed this approach and different kinds of core-shell heterostructures have been reported showing excellent electrochemical properties for supercapacitors. For instance, Zheng *et al.* reported the usage of $\text{MnCo}_2\text{O}_4@\text{MnO}_2$ core-shell nanowire arrays with mesoporous and large surface area grown directly on 3D nickel foam by hydrothermal method. The as fabricated electrode exhibits an enhanced specific capacitance of 858 F.g^{-1} at 1 A.g^{-1} when tested as supercapacitor electrode material.[62]

D. Research Objectives and Motivation

In order to apply advanced energy storage devices in commerce with high energy density and high-power density, supercapacitors still need to overcome some challenges. The largest obstacle for supercapacitors to compete batteries is their low energy density. Typically, pseudocapacitive materials are adopted to mitigate this problem. However, pseudocapacitive materials still suffer from low utility ratio. Thus, it is essential to design a rational structure to increase the contribution of pseudocapacitive materials, and meanwhile, provide effective electron and ion channels to achieve high power density. Nanotechnology has found potential and practical applications into various fields. In specific, nanostructuring electrode materials has been showing great efforts in solving such systematic problems. A lot of research groups and companies have taken the nanoscience advances into consideration in order to pave the way towards the coming generation of energy storage devices.

One of the main pillars into realizing high energy density for supercapacitors is by choosing the most suitable electrode materials, those that could provide high specific capacitance and cycling performance. At the same time, meeting the cost parameters and availability in nature. For instance, Ruthenium oxide (RuO_2) has been considered as an ideal supercapacitor electrode material, however with the high cost of such material, practical ap-

plications into research or industry seems to prevent the usage of ruthenium oxide in a wide spread. Generally, a supercapacitor electrode material should achieve the designated specifications of high specific capacitance, rate capability, good cycling and low costs with abundance in nature. Considering those facts, manganese cobalt oxides and nickel molybdate oxides were chosen as research objects for the application of supercapacitor devices. Moreover, rational design and nanostructure insights were key elements into the procedure of the conducted research.

1. Contents of Thesis

The main focus of this thesis is the study, design and fabrication of a high energy and power density asymmetric supercapacitor device based on a binder-free mixed metals core-shell heterostructure electrodes. Before the fabrication of the full supercapacitor, physical and electrochemical characterization were carried out on each individual synthesized material. The rate capability and specific capacitance of MnCo_2O_4 nanowire arrays were dramatically improved by applying an outer shell of NiMoO_4 nanosheets. The main contents of the thesis are as follows: Rational design of manganese cobalt oxide nanowires, nickel molybdate nanosheets through modified and simple hydrothermal methods. XRD, XPS, SEM, TEM and BET analysis and techniques were used to characterize and confirm the chemical composition and synergistic effects between active materials.

Firstly, electrochemical characterizations were carried out on the manganese cobalt oxide nanowires as a supercapacitor cathode material in a three-electrode system. Cyclic voltammetry, galvanostatic charge-discharge and long-term cycling stability of the manganese cobalt oxide were tested in the three-electrode system in 1 M KOH electrolyte. The manganese cobalt oxide nanowires displayed a specific capacitance of 457.85 F.g^{-1} at 1 A.g^{-1} and a 74% rate capability between $1-10 \text{ A.g}^{-1}$ capacitance range and a capacitance retention of 104% after 10000 cycles. The limited specific capacitance affects the energy density needed for fabricating a full supercapacitor device. The major focus of this study is to increase the specific capacitance of the manganese cobalt oxide by applying rational design and synthesis a nanostructure shell of nickel molybdate oxide sheets using the core manganese cobalt oxide as a scaffold.

The as-synthesized $\text{MnCo}_2\text{O}_4@\text{NiMoO}_4$ was electrochemically tested in a three-electrode system within 1 M KOH, and it exhibited excellent and improved performance when compared with single manganese cobalt oxide; a specific capacitance of 1244 F.g^{-1} at 1 A.g^{-1} with an extraordinary rate capability of 91% between $1-10 \text{ A.g}^{-1}$ capacitance range and a capacitance retention of 81% after 2500 successive cycles. For further comparison, NiMoO_4 nanosheets has been grown directly over the conductive substrate and tested separately with three-electrode system displaying a specific capacitance

of 762.5 F.g^{-1} at 1 A.g^{-1} and a 64% rate capability between $1\text{--}10 \text{ A.g}^{-1}$ capacitance range and a capacitance retention of 73% after 2500 cycles.

Using $\text{MnCo}_2\text{O}_4@\text{NiMoO}_4$ core-shell heterostructure with commercially available active carbon as positive and negative electrodes, respectively, we assembled and tested an asymmetric supercapacitor. The ASC device displayed high energy density of 42 W.h.kg^{-1} at a power density of 852.3 W.kg^{-1} . This work represents a promising rational nanostructured design for optimizing the electrochemical performance of asymmetric supercapacitor devices using synergistic effects between pseudocapacitive materials with extended reaction potentials.



Chapter II: Structural and Electrochemical Characterization Techniques

The increasing number of portable electronics in the world, which is becoming more than the number of the world population leads to increasing demand for energy storage components to power those devices. Such components would only be attractive to users if they have enough power to last at least several hours without being particularly heavy and expensive. Supercapacitors are one of those components that could provide high power density, but still lack the desirable energy density for industrial applications. Current research on supercapacitors is focused on increasing the energy density while conserving the high-power density and long cycle life.

By leveraging rational design principles for new nanostructured materials, there exists significant potential to achieve our design goals. Nanomaterials, typically ranging in size from 1 to 100 nm ($10\text{--}9$ meter) in at least one dimension, offer fascinating optical, electronic, and mechanical properties. Basic research in nanomaterials takes a material science-based approach to nanotechnology, benefiting from advancements in materials metrology and synthesis that have supported microfabrication research. At the nanoscale, we have observed intriguing phenomena that further enhance the appeal and potential of these materials.

There are two general approaches to the synthesis of nanomaterials and the fabrication of nanostructures. The bottom-up approach, which include the miniaturization of materials components (up to atomic level) with further self-assembly process leading to the formation of nanostructures. The physical forces operating at nanoscale during a self-assembly are used to combine basic units into larger stable structures. For instance, quantum dot formation during epitaxial growth and formation of nanoparticles from colloidal dispersion. On the other hand, top-down approach uses larger (macroscopic) initial structures, which can be externally con-

trolled in the processing of nanostructures. The typical examples of these approaches are etching through the mask, ball milling, hydrothermal and solvothermal methods. Among these fabrication methods, hydrothermal method is a facile and one of the most commonly used methods to synthesize nanomaterials for the application of supercapacitors.

2. Hydrothermal Synthesis Method

Hydrothermal synthesis is a solution reaction-based approach. In a broader sense, it can be defined as the method for making materials from room temperature to high-temperature solutions. To control the morphology of the materials to be prepared, either low pressure or high-pressure conditions may be used depending on the vapor pressure of the main composition in the reaction. Many types of nanomaterials have been successfully synthesized by the use of this approach. There are significant advantages of hydrothermal synthesis method over others. Hydrothermal synthesis can generate nanomaterials, which are not stable at elevated temperatures. Nanomaterials with high vapor pressures can be produced by the hydrothermal method with minimum loss of materials. The compositions of nanomaterials to be synthesized can be well controlled in hydrothermal synthesis through liquid phase or multiphase chemical reactions. By monitoring the time, concentration and temperature dependent reaction variables during hydrothermal synthesis, the size and morphology of nanostructures can be well controlled. The synthesis of MnCo_2O_4 nanowires and NiMoO_4 nanosheets was carried out through a facile hydrothermal method. A 100 ml Teflon-lined stainless-steel autoclave was used as the reactor for the hydrothermal synthesis of the MnCo_2O_4 and NiMoO_4 samples. For instance, NiMoO_4 mesoporous nanosheets have been prepared by a simple hydrothermal method using distilled water as a solvent at 160°C .[63] Various morphologies have been achieved and synthesized using the hydrothermal method for the application of supercapacitors. In specific, novel hierarchical core-shell structures have been previously reported using double steps of hydrothermal reactions, where at the first stage a scaffold structure

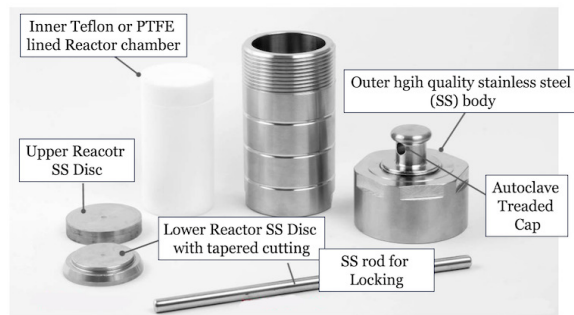


Figure 9. Teflon-lined stainless-steel reactor.

would be synthesized within the first reaction, followed by a second step of depositing an outer shell.[64]

3. Materials

The synthesis of MnCo_2O_4 nanowires was achieved through a facile hydrothermal method. The manganese cobalt nanowire arrays precursor obtained after the hydrothermal process were annealed in air at 350°C at a ramping rate of 1°C/min for 2 hours to improve the crystallinity of the material. For the synthesis of MnCo_2O_4 , Manganese (II) Nitrate Tetrahydrate ($\text{Mn}(\text{NO}_3)_2 \cdot 4\text{H}_2\text{O}$), Cobalt (II) Nitrate Hexahydrate ($\text{Co}(\text{NO}_3)_2 \cdot 6\text{H}_2\text{O}$), Ammonium Fluoride (NH_4F) and Urea ($\text{CH}_4\text{N}_2\text{O}$) chemical reagents were obtained from Sinopharm Chemical Reagent Co. Ltd and used as received. The synthesis of the heterostructure $\text{MnCo}_2\text{O}_4 @ \text{NiMoO}_4$ core-shell nanowire arrays were also achieved by a simple hydrothermal method and post-annealing treatment in Aragon atmosphere at 350°C at a ramping rate of 1°C/min for 5 hours. For this synthesis, Sodium Molybdate Dihydrate ($\text{Na}_2\text{MoO}_4 \cdot 2\text{H}_2\text{O}$) and Nickel (II) Nitrate Hexahydrate ($\text{Ni}(\text{NO}_3)_2 \cdot 6\text{H}_2\text{O}$) was purchased from Sinopharm Chemical Reagent Co. Ltd. The chemical reagents were used without any further purification. All electrochemical tests were carried out in 1 M KOH electrolyte. Potassium hydroxide (KOH) chemical reagent was purchased from Sinopharm Chemical Reagent Co. Ltd and used as received.

4. Synthesis Equipment and Instrumentation

The synthesis of the cathode and anode materials were carried out in the wet laboratory with the listed equipment and instruments. Based on stoichiometric calculations, the amounts of the different reagents were measured with an analytical balance (BS124s) manufactured by Sartorius Ltd. A magnetic stirrer (78HW-1) was used to stir and dissolve the chemical reagents in double distilled water ($18.2 \text{ M}\Omega \cdot \text{cm}^2$). The precursor solutions were transferred into a Teflon lined stainless steel autoclave and heated in a blast oven (DGG-9070A). Annealing of the MnCo_2O_4 nanowires and $\text{MnCo}_2\text{O}_4 @ \text{NiMoO}_4$ core-shell nanowire arrays was carried out with a tubular furnace (SX-G02125).

E. Experimental Procedure

1. Synthesis Method of MnCo_2O_4 Nanowires

The synthesis of MnCo_2O_4 nanowires was achieved through a modified facile hydrothermal method and post-annealing treatment [Fig. 10]. The reaction solution was obtained by dissolving 1 mmol $\text{Mn}(\text{NO}_3)_2 \cdot 4\text{H}_2\text{O}$ (0.25 g), 2 mmol $\text{Co}(\text{NO}_3)_2 \cdot 6\text{H}_2\text{O}$ (0.58 g), 6 mmol NH_4F (0.22 g)

and 15 mmol Urea (0.9 g) in 70 ml of distilled water by the aid of magnetic stirring for 30 min at room temperature (RT). Afterwards, the resulting clear pink solution was transferred into a Teflon-lined stainless-steel autoclave. A pre-treated nickel foam (NF) was immersed into the reaction solution and the hydrothermal process was carried out at 120°C for 4h. After cooling down to room temperature, the cobalt-manganese hydroxide precursor film was removed and washed thoroughly with deionized water and ethanol absolute for several times and dried at 70°C for 12h. Finally, the precursor film was annealed at 350°C in Air for 2h and ramping rate of 1°C/min to obtain MnCo_2O_4 nanowire heterostructure array with an active material mass loading of $\sim 2 \text{ mg.cm}^{-2}$.

2. Synthesis of heterostructure $\text{MnCo}_2\text{O}_4 @ \text{NiMoO}_4$ core-shell nanowire arrays

A second hydrothermal process was carried out in order to deposit an outer shell of NiMoO_4 nanosheets using the previous MnCo_2O_4 nanowires as a scaffold with post-annealing treatment in Aragon atmosphere [Fig. 11]. A second hydrothermal process was carried out to synthesize the $\text{MnCo}_2\text{O}_4 @ \text{NiMoO}_4$ core-shell hybrid arrays where 70 ml mixed solution of 1mmol $\text{Na}_2\text{MoO}_4 \cdot 2\text{H}_2\text{O}$ (0.242g) and 1 mmol $\text{Ni}(\text{NO}_3)_2 \cdot 6\text{H}_2\text{O}$ were added to Teflon-lined stainless-steel autoclave containing Ni foam supported MnCo_2O_4 nanowire heterostructure arrays. The autoclave was maintained at 120°C for 6h. Afterwards, the autoclave was cooled down to RT, and then the sample was removed and washed thoroughly with deionized water and ethanol absolute. After drying for 12h at 70°C, the sample was annealed at 350°C for 5h in Aragon atmosphere at a ramping rate of 1°C/min. The mass loading of active material after calcination is $\sim 5 \text{ mg/cm}^2$. For comparison, bare NiMoO_4 on Ni foam was also prepared using the same method.

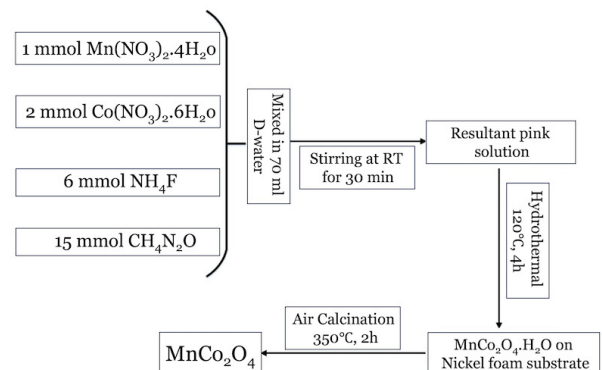


Figure 10. Hydrothermal synthesis of MnCo_2O_4 nanowire arrays.

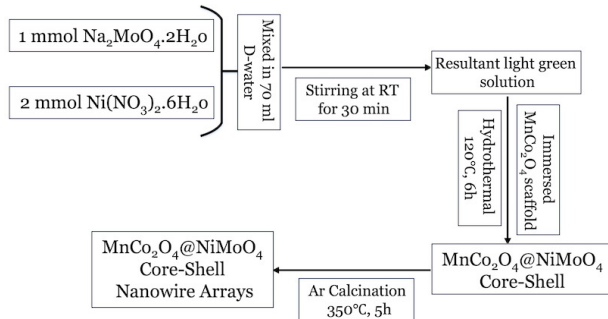


Figure 11. Hydrothermal synthesis of $\text{MnCo}_2\text{O}_4@\text{NiMoO}_4$ core-shell heterostructure.

F. Physical Characterizations

Characterization techniques are key elements for nanostructured electrode materials design; they play a fundamental role in understanding the mechanisms and realizing the basic concepts of nanoscale architectures. Such techniques essential for researchers to recognize if they have achieved the expected materials and structures. The good understanding of these techniques, including advantages and limitations, is necessary to evaluate any work related to nanomaterials and nanoscience. In the following chapter, we will list the major characterization techniques involved in this study, along with a brief description.

1. X-Ray Diffraction (XRD)

X-ray powder diffraction (XRD) is a rapid analytical technique, primarily used for phase identification of a crystalline material and can provide information on unit cell dimensions. The analyzed material is finally ground, homogenized, and average bulk composition is determined. X-ray is based on constructive interference of monochromatic X-rays and a crystalline sample. The X-rays are generated by a cathode ray tube, filtered to produce monochromatic radiation, collimated to concentrate, and directed toward the sample. The interaction of the incident rays with the sample produces constructive interference (and a diffracted ray) when conditions satisfy Bragg's law $n\lambda = 2ds\sin(\theta)$. According to Bragg's law, there is a relation between the wavelength of electromagnetic radiation, the diffraction angle, and the lattice spacing in a crystalline sample. The diffracted X-rays are then detected, processed and counted. XRD as a characterization technique has some advantages and limitations, the advantages of XRD is that it is a powerful and rapid technique (< 20 min) for identification of an unknown mineral, minimal sample preparation is required, as well as the interpretation of obtained data is relatively straight forward. On the other hand, XRD has some limitations. For instance, only homogeneous and single-

phase materials will be best identified, and for mixed materials, detection limit is 2% of sample. Peak overlay may occur and worsens for high angle reflections. The crystallographic phases and crystallinity of the samples were identified through the XRD tests. The characterization was performed with a Bruker D8 Advance X-ray diffractometer with a non-monochromatic Cu K α X-ray source.

2. Scanning Electron Microscopy (SEM)

Scanning Electron Microscopy (SEM) is an imaging technique used to observe the topography and surface of a sample using electron beams. An effective instrument that allows researchers to unveil the morphology and the structure of micro- and nanoscale materials. The general configuration of an SEM is shown in [Fig. 12]. As we can see, SEM is column in shape, has an electron gun on the top of the column, which can produce electrons with the energy of 0.1–30 keV. After that, we have the condenser lens, apertures, and objective lens that is used to concentrate the electron beam and focus it on the specimen. In order to prevent the electrons from being scattered by air, a high-vacuum atmosphere with less than 10–5 mbar is created. The electrons in the beam will interact with the sample and lose energy by repeated random scattering and adsorption. High-energy electrons are reflected due to elastic scattering, while secondary electrons are generated from inelastic scattering in the sample. Detectors are placed around the sample, the energy is measured before collecting the images. By rastering the beam onto the surface of the sample, the topology can be identified. One of the biggest limitations of SEM is that imaging via this technique requires the use of a vacuum atmosphere due to the necessity of generating an electron beam. As well as, the elevated energy of the beam may destroy fragile samples, and this must be taken into account when preparing samples. The SEM images were taken at high (200 nm) and low magnifications (1 μm) to provide important information about the core-shell morphology of the samples. The accelerating voltage is set to 15 kV and a minimum vacuum pressure requirement

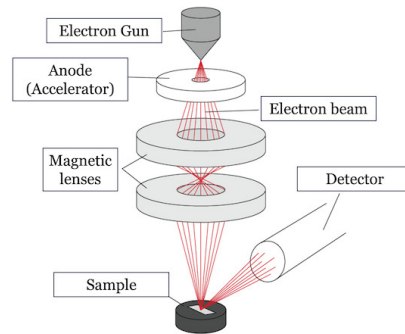


Figure 12. Schematic view of a scanning electron microscope.

of 9.6×10^{-5} Pa.

4. X-Ray Photoelectron Spectroscopy (XPS)

X-ray Photoelectron Spectroscopy (XPS) also known as Electron Spectroscopy for Chemical Analysis (ESCA) is the most widely used surface analysis technique because it can be applied to a broad range of materials and provides valuable quantitative and chemical state information from the surface of the material being studied. The average depth of analysis for an XPS measurement is approximately 10 nm. To analyze the bulk of a material, some treatment is necessary such as fracturing, cutting, and scraping to remove the contamination on the surface and expose the deep layer for further characterization. XPS requires high vacuum atmosphere, and when irradiating the sample material by X-ray beam, the electrons on the surface of the material will escape, so that we will be able to measure the number and kinetic energy of the electrons. The binding energy can be determined by the following equation:

$$E_{binding} = E_{photon} - E_{kinetic} - \Phi \quad (3)$$

Where $E_{kinetic}$ is the kinetic energy of the escaped electrons, E_{photon} is the energy of incident X-ray photon, and Φ is the work function, which depends on both spectrometer and the material. The schematic illustration in [Fig. 14] shows the basic configuration of XPS measurement. One of the basic advantages of XPS over other surface characterization techniques is the usage of X-rays instead of electron beams (like other techniques such as AES or EDS), for that, the XPS analysis does less damage to the sample surface than other surface analysis techniques. This is of vital importance for supercapacitor research, where a device must be constructed after the surface chemistry has been analyzed. Another key advantage of XPS is its ability to inform the researcher about the nature of the chemical bonding and valence states of the elements within the sample. On the other hand, this technique has some drawbacks. Firstly, XPS is very sensitive to the ambient atmosphere, an inert atmosphere sample-preparation box is usually required to prepare the samples and load them into the instrument. Secondly, the identification of XPS peaks as specific bonds. In order to do this, the experimental spectra are usually compared with a large database of stored

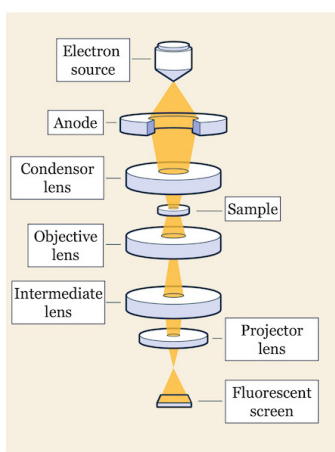


Figure 13. Schematic view of a transmission electron microscope.

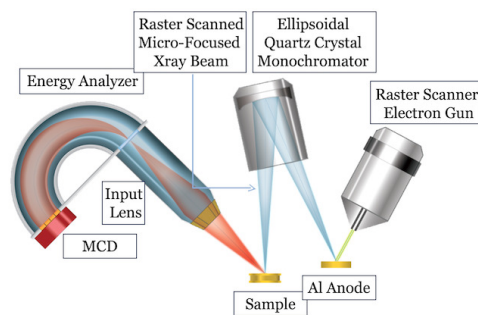


Figure 14. Schematic view of the configuration of the XPS.

identified spectra. X-ray Spectroscopy analysis was done with a VG Multite 2000 to determine the oxidation states of the $\text{MnCo}_2\text{O}_4@\text{NiMoO}_4$ core-shell heterostructure.

5. Nitrogen Adsorption–Desorption Isotherm Technique

Nitrogen adsorption-desorption isotherm technique is a powerful tool to identify the surface area and pore volume of porous materials. The adsorption-desorption is carried out at very low temperature, around the boiling temperature of liquid nitrogen. Generally, the adsorption of gas molecules on solid surface is reversible because of the weak physical van der Waals (vdW) interaction. As we can see in [Fig. 15]. The first type of isotherms is Type I, which is an indicator of microporous existence in a material. Type II isotherm indicates non-porous materials. Type III isotherm shows a typical plot of vapor adsorption. Type IV and V isotherms with hysteresis loop indicates the presence of capillary condensation in mesoporous materials. Lastly, type VI usually occurs in special carbon. We can obtain the specific surface area by nitrogen adsorption/desorption method based on the theory of BET, which is an extension of Langmuir theory. The principle of BET theory is shown by the following equation:

$$\frac{1}{v[(\frac{p_0}{p})] - 1} = \frac{c - 1}{v_m c} \left(\frac{p_0}{p} \right) + \frac{1}{v_m c} \quad (4)$$

Where v is the volume of absorbed gas, p is equilibrium pressure, p_0 is saturation pressure, v_m is the volume of monolayer-absorbed gas, and c is the BET constant. The final specific surface area (BET surface area) can be determined by the following equation:

$$S_{BET} = \frac{(v_m N s)}{V a} \quad (5)$$

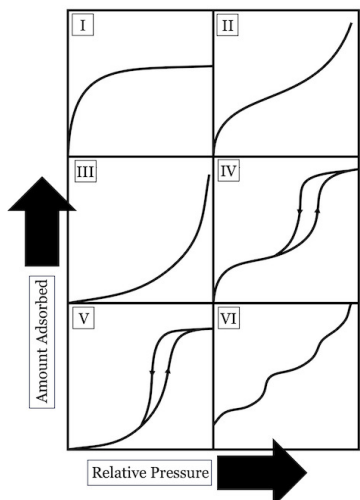


Figure 15. Schematic view of different types of nitrogen adsorption/desorption isotherms.

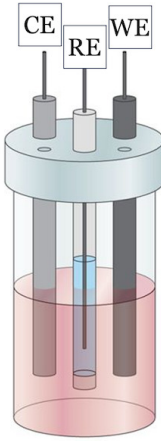


Figure 16. Schematic view of three electrode (half-cell) configuration.

Where v_m is molar volume of the monolayer adsorbed gas, N is the Avogadro's number, s is the cross-section of the adsorbing species, V is the molar volume of absorbed gas, while a is the mass of adsorbent. BET experimental procedure is divided into adsorption and desorption tests. The analysis of the absorption and desorption isotherms provides total specific surface area (usually $\text{m}^2 \text{ g}^{-1}$). It also allows determination of pore size distribution. The BET test was conducted with Tristar II 3020 under liquid nitrogen (77 K) testing conditions. The mass of the samples for the BET test met the minimum requirement of 100 mg. Prior to testing the BET surface area, the samples were first degassed fully at 150°C for 12 hours to get rid of all gases present in the sample.

G. Electrochemical Characterization

In order to evaluate the electrochemical performance of supercapacitor electrode materials, electrochemical characterization techniques such as cyclic voltammetry (CV), galvanostatic charge/discharge (GCD), and electrochemical impedance spectroscopy (EIS) are applied. A high-performance supercapacitor electrode material should have a good rate capability, high specific capacitance, and low electrical resistance.

Two-cell configurations are used for characterizing the supercapacitor electrode material. Firstly, the half-cell configuration shown in [Fig. 16], in which a three-electrode system is used, which consists of a working electrode, counter electrode, and a reference electrode. The active electrode is used as the working electrode. In order to record the potential of this working electrode, a reference electrode whose potential is almost constant in a narrow potential range is used. In addition, a counter electrode, which is usually a platinum wire, is also necessary to carry the current coming across from the working electrode, which can prevent the reference electrode from carrying current, leading to potential change of the ref-

erence electrode.

Secondly, full cell configuration, which is usually used in a two-electrode system. The full cell configuration can show more practical performance of active materials than half-cells, because full cell test works similar to a practical supercapacitor. In a full cell configuration, both electrodes (the positive and negative electrodes) are assembled with active materials. According to the similarity between the two active materials, supercapacitors can be divided into symmetric and asymmetric supercapacitors, respectively. In general, the maximum total capacitance of the full cell is achieved when two electrodes have the same capacitance. Thus, it is significant to control the mass loading of each electrode to meet a high total capacitance.

1. Cyclic Voltammetry (CV)

Cyclic voltammetry is one of the most applied characterization techniques to study the electrochemical performance of supercapacitor electrode materials. In this technique, a potential on the working electrode ramps linearly with time, starting from the open circuit potential to a set potential. After that, the potential returns to the other set potential in the same way, in what we call a *sweep cycle*. During that, both scan rate and number of cycles can be controlled. In order to analyze the electrochemical properties of the material, the redox potential of the active material should be contained within the potential window of CV. [Fig. 17] Shows a typical cyclic voltammogram. As we can see, the corresponding current is a function of the scanning potential. We can use the cyclic voltammogram to get information about the chemical reaction, the capacitance, polarization, and the position of redox peaks. By using the area under the CV curve, we can calculate the specific capacitance of the active material with the following equation:

$$C = \frac{1}{2} \left(\frac{\int idv}{mvU} \right) \quad (6)$$

Where C is the specific capacitance. m is the mass loading of active material, U is the potential window, v is the scan rate, and $\int idv$ is the area under the CV curve. As a

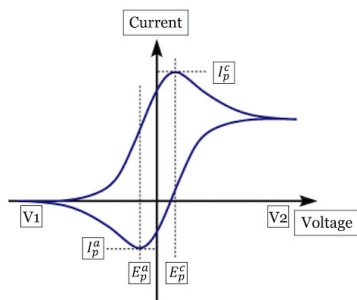


Figure 17. Schematic view of a typical cyclic voltammogram.

single cycle with the CV curve contains both charge and discharge processes, the entire area should be divided by two in order to obtain the specific capacitance.

2. Galvanostatic Charge and Discharge (GCD)

For more accurate evaluation of specific capacitance of an active material than the CV method, galvanostatic charge and discharge is applied. In this method, positive and negative constant currents come across the working electrode to charge and discharge the electrode in a set voltage range with recording time. A typical GCD curve is shown in [Fig. 18]. As we can see the voltage is plotted as a function of the time. The specific capacitance can be determined using the following equation:

$$C = \frac{I\Delta t}{mU} \quad (7)$$

Where I is the current, Δt is the discharge time, m is the mass loading of active material, and U is the potential window.

3. Electrochemical Impedance Spectroscopy (EIS)

Electrochemical impedance spectroscopy is one of the important methods to analyze the impedance in an electrochemical system. An alternating potential with changing frequency is applied onto the system, so that we will be able to test the ratio of alternating potential to the corresponding current signal as a function of sinusoidal wave frequency. Herein, the impedance that will result from the quotient of potential divided by current is a complex number. We can use this complex value to obtain the Nyquist plot, by using the real part as x -axis and the imaginary part as y -axis. Nyquist plot will help the researcher in analyzing the electrochemical impedance. [Fig. 19] shows a typical Nyquist plot. This plot is consisted of a semicircle followed by a 45° straight line. The interception on x -axis at high frequency region represents

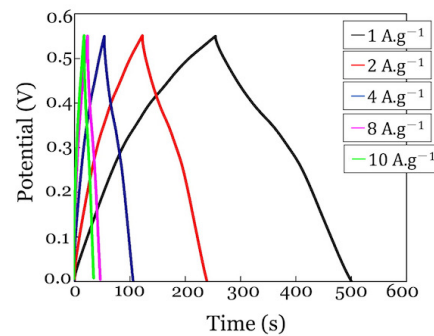


Figure 18. Galvanostatic charge-discharge profile of MnCo_2O_4 with the voltage range from 0 to 0.6 V vs. saturated calomel electrode (SCE) at different current densities.

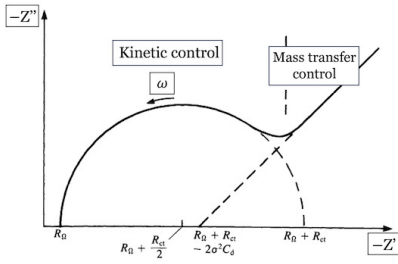


Figure 19. Schematic view of a typical Nyquist plot used to analyze the electrochemical impedance of an electrochemical system.

the serial resistance of the electrode, whereas the semi-circle region reflects the charge transfer resistance that is related to reactive kinetics. For the low frequency part, that 45° straight line is well known as "Warburg" diffusion region, which is attributed to the diffusion transmission resistance in the electrode. If the EIS curve is more complex, for that case the electrochemical system should be represented by an equivalent circuit and then analyzed by circuit modeling software.

In our study, the cyclic voltammetry was used to investigate and obtain quantitative and qualitative data about the electrochemical reactions such as the reaction mechanisms, electrochemical kinetics and reaction reversibility. The cyclic voltammetry tests of the prepared samples were tested with a CHI 760D electrochemical workstation. The cyclic voltammetry of $\text{MnCo}_2\text{O}_4@\text{NiMoO}_4$ nanowires were tested in a 0–0.6 V potential range, while the cyclic voltammetry curves of the full device $\text{MnCo}_2\text{O}_4@\text{NiMoO}_4//\text{AC}$ were tested in a 0–1.6 V potential range. Galvanostatic charge-discharge cycles were performed with a CHI 760D electrochemical workstation. The specific capacitances of the electrodes at different current densities were calculated from the galvanostatic discharge curves.

The Electrochemical impedance spectroscopy of the electrodes was measured with a CHI 760D electrochemical workstation over a 0.01 Hz to 10 kHz frequency range at an open-circuit potential with an AC amplitude of 10 mV. Electrochemical impedance spectroscopy provides information about the charge transfer resistance (R_{ct}), bulk resistance (R_s) and the reaction transfer kinetics. The main formulas used in calculating the specific capacitance, the energy density and the power density are the following:

- Calculation of specific capacitance: The specific capacitances of the electrodes and devices were calculated from the galvanostatic charge-discharge curves according to the following equation:

$$C = \frac{I \times \Delta t}{m \times \Delta V} \quad (8)$$

Where C (F.g^{-1}) is the specific capacitance, I is the discharge current, Δt is the discharge time and

m is the mass loading of the active materials grown on the conductive substrates (nickel foam), ΔV is the voltage range excluding the potential drop.

- Balance of charge for the as-assembled ASC: The mass ratio of the positive to negative electrode is obtained by using the following equation:

$$\frac{m_+}{m_-} = \frac{C_- \times \Delta V_-}{C_+ \times \Delta V_+} \quad (9)$$

Where m_+ and m_- are the mass loading of the positive and negative electrodes, respectively, C_+ and C_- are the specific capacitance of the positive and negative electrodes, respectively. ΔV_+ and ΔV_- are the voltage window of the positive and negative electrodes, respectively.

- Energy and power density: The energy and power density of the as-fabricated asymmetric supercapacitor were calculated based on the formula:

$$E = \frac{\int IV(t) dt}{m} \quad (10)$$

$$P = \frac{E}{\Delta t} \quad (11)$$

Where E (W.h.kg^{-1}) is the energy density, P (W.kg^{-1}) is the power density, I is the discharge current, $V(t)$ is the discharge voltage excluding the IR drop, m is the total mass of the active material (cathode and anode), dt is the time differential and Δt is the discharge time.

- Preparation of electrodes: A $1 \times 1 \text{ cm}^2$ piece of $\text{MnCo}_2\text{O}_4@\text{NiMoO}_4$ core-shell nanowire arrays (mass loading: 5 mg) grown on the conductive substrates (Nickel Foam) were used as working electrodes for the electrochemical performance tests. The mass loading of the different electrodes were determined as follows; nickel foam ($2 \times 5 \text{ cm}^2$) initially weighed prior to the hydrothermal growth process. All the samples were washed with distilled water and absolute ethanol, and then dried thoroughly at 70°C overnight before being weighed with an analytical balance. The mass of the active materials was determined by the mass difference (before and after calcination of the cathode) divided by the macroscopic area of the conductive substrates.



Chapter III: One-dimensional MnCo_2O_4 Nanowire Arrays for Supercapacitor Applications

It is well believed that transition metal oxides with various nanostructures are promising electrode materials for supercapacitor applications because of their

high specific capacitance, especially when compared with carbon based materials.[65] In recent studies, binary metal oxides such as spinel cobaltites (MCo_2O_4 ; $M = Mn, Ni, Zn, Cu, etc.$) have been documented to possess superior electrochemical performance to single or mono metal oxides.[33] For example, binary manganese cobaltite ($MnCo_2O_4$) has shown higher electrochemical activity and better electrical conductivity than unitary cobalt oxide (Co_3O_4) and manganese oxide (MnO_2).[66] However, there still exist some drawbacks, such as relatively low conductivity, low utilization of active materials and inferior structure stability. One of the remarkable solutions to this problem is using nanostructures design, in specific the 1D nanowire arrays, because of their excellent physical and chemical properties as they can provide large specific surface area, which results in high utilization of active material.

Herein, 1D $MnCo_2O_4$ nanowire arrays grown on a substrate of nickel foam by a hydrothermal method, followed by post-annealing procedure as shown in [Fig. 20] is studied and investigated as a cathode material for supercapacitors. The $MnCo_2O_4$ nanowires are crystalline and exhibit good electrochemical performance with a specific capacitance of 457.85 F.g^{-1} at 1 A.g^{-1} and 340.6 F.g^{-1} at 10 A.g^{-1} with an outstanding cycling stability of $\sim 104\%$ after 10000 cycles. The good electrochemical performance of the $MnCo_2O_4$ NWAs is mainly attributed to the special nanowire structure, which provides large surface area for electrochemical reactions, fast ion and electron transfer and good structure stability. In this chapter, we go through the process of preparing and evaluating manganese cobalt oxide nanowire arrays as a cathode for supercapacitors, which has been grown over a conductive substrate of nickel foam by a facile and modified hydrothermal method, followed by a calcination treatment in Air condition.

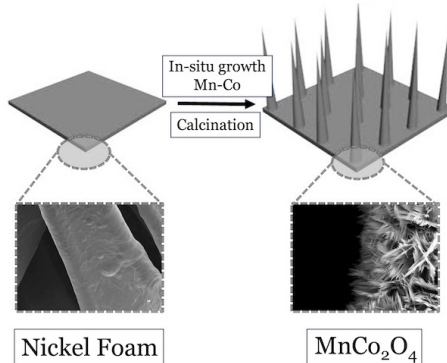


Figure 20. Schematic illustration of the fabrication process of the $MnCo_2O_4$ nanowire arrays over the nickel foam.

H. Experimental Procedure

1. Synthesis of $MnCo_2O_4$ Hetero-Nanostructures

The reaction solution was obtained by dissolving 1 mmol $Mn(NO_3)_2 \cdot 4H_2O$ (0.25 g), 2 mmol $Co(NO_3)_2 \cdot 6H_2O$ (0.58 g), 6 mmol NH_4F (0.22 g) and 15 mmol Urea (0.9 g) in 70 ml of distilled water by the aid of magnetic stirring for 30 min at RT. Afterwards, the resulting clear solution was transferred into a Teflon-lined stainless-steel autoclave. A pre-treated nickel foam was immersed into the reaction solution and the hydrothermal process was carried out at $120^\circ C$ for 4h. After cooling down to room temperature, the cobalt-manganese hydroxide precursor film was removed and washed thoroughly with deionized water and ethanol absolute for several times and dried at $70^\circ C$ for 12h. Finally, the precursor film was annealed at $350^\circ C$ in Air for 2h and ramping rate of $1^\circ C/\text{min}$ to obtain $MnCo_2O_4$ nanowire heterostructure array with a mass loading of $\sim 2\text{ mg.cm}^{-2}$.

2. Characterization

The crystallographic characterization of the as-synthesized samples was performed with a Bruker D8 Advance X-ray diffractometer with non-monochromatic Cu Ka X-ray source. Field emission scanning electron microscopy (SEM) images were obtained with a JEOL-7100F microscope. Transmission electron microscopy (TEM) images were collected with a JEM-2100F STEM/EDS microscope. The Brunauer-Emmett-Teller (BET) surface area was measured using a Tristar II 3,020 instrument at 77K. X-ray photoelectron spectroscopy (XPS) measurements were carried out using a VG Multi Lab 2000 instrument.

3. Electrochemical Measurements

The electrochemical measurements of the individual electrode samples were performed using a three-electrode cell system with the as-synthesized materials on the conductive substrates as the working electrode, saturated calomel electrode (SCE) as reference electrode and platinum (Pt) plate as counter-electrode in a 1 M KOH electrolyte using an electrochemical workstation (CHI760E). The specific capacitances of the electrodes and devices were calculated from the galvanostatic discharge curves at different current densities using the following formula:

$$C_s = \frac{I \times \Delta t}{m \times \Delta V} \quad (12)$$

Where C_s (F.g^{-1}) is the specific capacitance, I (A) is the discharge current, Δt (s) is the discharge time, m (g) is the mass of the active material and ΔV is the operating voltage (calculated from the discharge curves excluding the potential drop).

I. MnCo₂O₄ Nanowire Arrays (NWAs)

As has been illustrated in [Fig. 20], the first stage in the synthesis of MnCo₂O₄ includes an in-situ growth of precursor nanowires on a pre-treated nickel foam substrate.

1. XRD and XPS Characterization of MnCo₂O₄

In order to investigate the crystal structure and chemical composition of the as synthesized material, XRD and XPS analysis were conducted using the powder scratched out of the substrate. As shown in [Fig. 21], the diffraction peaks can be well indexed with the face-centered-cubic (FCC) spinel structure of MnCo₂O₄ (JCPDS card no.01-1130).[66] The full scan survey spectrum of the MnCo₂O₄ with corresponding peaks are shown in [Fig. 22 (a)], indicates the presence of Mn, Co, and O elements. The Mn 2p core spectrum shown in [Fig. 22 (b)] can be deconvoluted into two peaks, Mn 2p_{3/2} and 2p_{1/2} with binding energies of 642.5 and 653.7 eV, respectively, indicating a tetravalent state of Mn.[67] Co 2p_{3/2} and Co 2p_{1/2} peaks which are characteristic of Co²⁺ and Co³⁺ are located at binding energies of 781.2 and 797.6 eV, respectively from the deconvolution of the Co 2p peak in [Fig. 22 (c)].[68] Lastly, the deconvolution of O 1s core-level spectrum in [Fig. 22 (d)] shows two peaks. The peak located at 530.8 eV is associated with the metal-oxygen bonding (oxygen binding with Mn and Co), while the other peak at 532 eV can be attributed to oxygen ions in low coordination at the surface.[69]

2. Growth Mechanism of MnCo₂O₄ NWAs

The growth mechanism of the as-prepared material over the nickel foam substrate was investigated through the morphology evolution vs time of hydrothermal growth procedure, where morphology was studied after 1, 2 and 4 hours. It is well known that nanowires have been grown through many methods, such as electrochemistry, templates (mesoporous silica, carbon nanotubes, etc.), emulsion or polymeric systems, arc discharge and

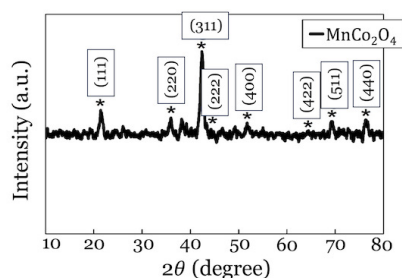


Figure 21. XRD pattern of MnCo₂O₄ powders scratched off the Ni foam.

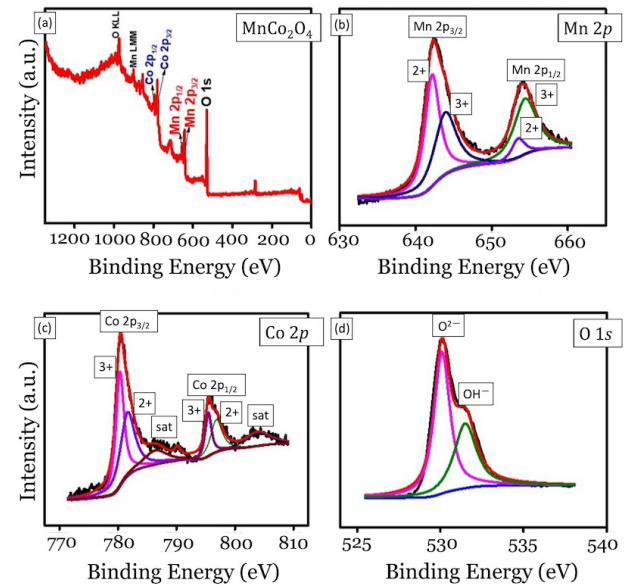


Figure 22. (a) XPS spectra of as-synthesized MnCo₂O₄ NWAs, (b-d) XPS survey scan of Mn 2p, Co 2p and O 1s regions, respectively.

laser-assisted catalytic growth, solution and vapor transport methods.[70] Controlling the synthesis of nanowires could be affected by different aspects, which has an important effect on the hydrothermal method. For instance, materials with highly anisotropic crystal structures will easily grow into 1D nanowires, a phenomenon that is determined by the highly anisotropic bonding in the crystallographic structure. Usually the crystallization tends to occur along a certain axis. In addition, the solvents used in the hydrothermal synthesis have proved to have key effects in the formation of nanowires, where they serve as the structure directing coordination (template effect) during nanowires formation. For the shapes of nanocrystals, they could be defined by the relatively specific surface energies associated with facets of the crystal. One can control the final shape of a crystal by introducing appropriate surfactants/capping reagents to change the free energies of the various crystallographic surfaces and thus to alter their growth rates. In our study, ammonium florid and urea were used as surfactant and capping agents. By controlling the concentration of reaction agents and duration of hydrothermal process, we were able to get well-defined arrays of nanowires. [Fig. 23 (a)] shows that after 1 hour of hydrothermal reaction, a semi-hexagon base structure starts to form. By increasing the reaction time up to 2 hours, the nanowires heterostructure tends to grow out of the semi-hexagon base as shown in [Fig. 23 (b)]. As we can see, the nanowires still don't have an even shape. However, by increasing the reaction time to reach 4 hours we were able to get a well-covered substrate with evenly shaped nanowire arrays.

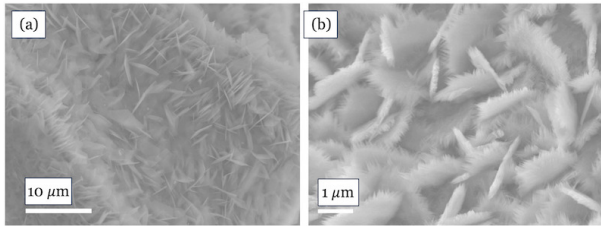


Figure 23. Typical (a) and (b) SEM images of $MnCo_2O_4$ nanowires growth procedure with different reaction time duration (1 hour and 2 hours), respectively.

3. Morphology Characterization of $MnCo_2O_4$ NWAs

The morphology of $MnCo_2O_4$ nanowires was examined by top-view field emission scanning electronic microscopy (FESEM, JOEL-7100F) at an acceleration voltage of 15 kV and TEM measurement by means of JEM-2100F instrument was used to get further insight of the synthesized material. 3D $MnCo_2O_4$ heterostructure NWAs was grown directly on Ni foam through a facile modified hydrothermal process followed by annealing process as shown in schematic [Fig. 20]. The nanowire morphology was identified by SEM as shown in [Fig. 24]. As we can see in [Fig. 24 (a)], the panoramic view shows that the $MnCo_2O_4$ NWAs are grown tightly with high coverage density over the Ni foam substrate. [Fig. 24 (b)], shows that a single nanowire has an average diameter of 100 nm and an average length of 2 μm , which could increase the specific surface area and shorten the ion-diffusion pathways. The inset in [Fig. 24 (b)], we can observe the existence of plenty of space in-between the nanowires, which could effectively enhance the contact between the electrode material and electrolyte. The typical TEM images of $MnCo_2O_4$ nanowires are shown in [Fig. 25]. We can observe that a single nanowire is composed of smaller nanoparticles with an average size of ~ 13 nm and has a diameter of 100 nm, which is consisted with the SEM results. Two clear lattice fringes with fringe spacing of 0.47 and 0.23 nm corresponding to the (111) and (222) planes of $MnCo_2O_4$, respectively, are observed and de-

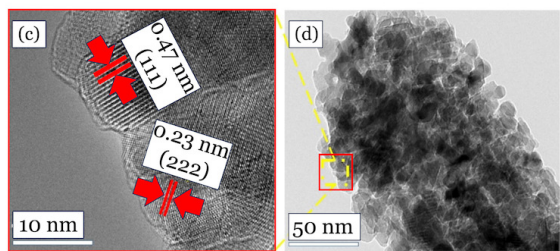
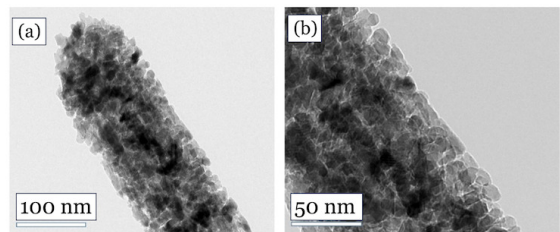


Figure 25. Typical (a), (b), and (d) TEM images of a single $MnCo_2O_4$ nanowire, (c) HRTEM image of single $MnCo_2O_4$ nanowire.

picted in Figure [Fig. 25 (c)]. Furthermore, energy dispersive X-ray spectroscopy (EDS) mapping was observed with a JOEL-7100F. the EDS elemental mapping of the manganese cobalt nanowires is shown in [Fig. 26]. The elemental mapping shows the uniform distribution of Mn and Co elements along each single nanowire, which is in good agreement with the XRD and XPS spectroscopy. To further investigate the surface area and pore size distribution of the as-synthesized $MnCo_2O_4$, BET analysis have been conducted as shown in [Fig. 27]. The $MnCo_2O_4$ NWAs shows a type II isotherm with a very low adsorbed amount at low pressures and almost negligible desorption loop, which indicates an almost non-porous feature of the material. The estimated BET sur-

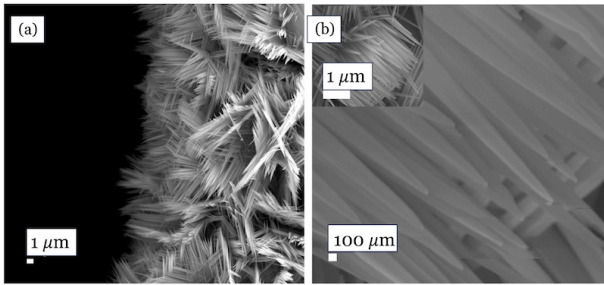


Figure 24. (a) Panoramic view of $MnCo_2O_4$ NWAs grown directly over Ni foam, (b) Typical SEM images with high magnification and (inset) low magnification of $MnCo_2O_4$ NWAs.

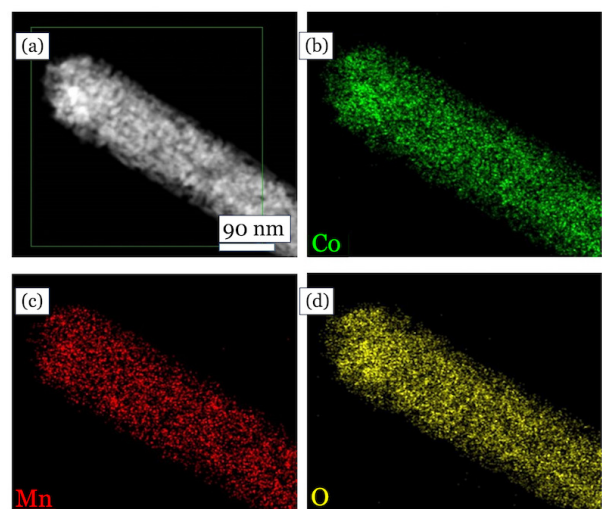


Figure 26. (a) Demonstrating $MnCo_2O_4$ hierarchical structure of a single nanowire, (b-d) corresponding EDS mapping.

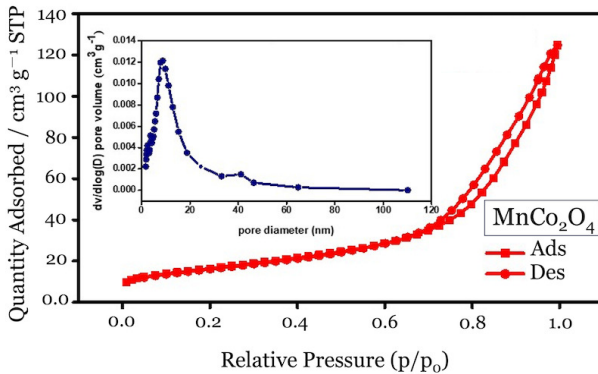


Figure 27. N_2 adsorption-desorption isotherms and corresponding pore size distribution curves of MnCo_2O_4 .

face area of MnCo_2O_4 is $59 \text{ m}^2/\text{g}$. with regard to the pore size distribution in inset [Fig. 27], the pore sizes are distributed nearby 10 nm.

4. Electrochemical Characterization of MnCo_2O_4 NWAs

In order to evaluate the validity of the fabricated material for supercapacitor applications, MnCo_2O_4 was tested as a working electrode using a three-electrode cell system with as synthesized material as the working electrode, SCE as reference electrode and Pt plate as counter electrode in a 1 M KOH electrolyte. [Fig. 28 (a)] shows the CV curves of MnCo_2O_4 NWAs electrode in the potential range 0–0.5 V (Ag/AgCl) at different scan rates. As we can see, a pair of redox peaks are observed within the anodic and cathodic processes, which is an indicator of faradic behavior. The redox reaction mechanism is described by the following equations, and the chemical transformations are highly reversible:[71]

$$\text{MnCo}_2\text{O}_4 + \text{H}_2\text{O} + \text{OH}^- \rightarrow 2\text{CoOOH} + \text{MnOOH} + \text{e}^-$$

$$\text{MnOOH} + \text{OH}^- \rightarrow \text{MnO}_2 + \text{H}_2\text{O} + \text{e}^-$$

[Fig. 28 (b)] shows the galvanostatic charge/discharge curves of MnCo_2O_4 nanowire arrays in a potential range of 0–0.6 at different current densities ranging from 1 to 10 A.g^{-1} . Accordingly, the specific capacitance of the MnCo_2O_4 NWAs is calculated to be 457.85 F.g^{-1} at 1 A.g^{-1} . [Fig. 28 (c)], shows the specific capacitances of MnCo_2O_4 electrode calculated at different current densities, when increasing the current density to 10 A.g^{-1} , the specific capacitance dropped down to be 340.6 F.g^{-1} , and for that only 74% of the capacitance is maintained when the discharge current density increases from 1 A.g^{-1} to 10 A.g^{-1} . In order to evaluate the cycling performance of as-synthesized material, successive charge-discharge tests have been conducted at a current density of 1 A.g^{-1} for 10000 cycles. [Fig. 28 (d)], shows that MnCo_2O_4 still delivers a high capacitance after 10000 cycles retaining more than 100% of its initial capacitance, indicating a remarkable cycling stability. Furthermore, we checked the morphologies of the nanowires after the

cycling test and we found that it was well preserved with ignorable changes on the surface of the nanowires as it is shown in [Fig. 29]. To further understand the outstanding cycling stability, electrochemical impedance spectroscopy (EIS) was carried out over a 0.01 Hz to 105 Hz frequency range at an open-circuit potential with an AC amplitude of 5 mV. [Fig. 30] displays the Nyquist plot of the MnCo_2O_4 nanowires tested before, during, and after cycling. It can be observed that the slope in the low-frequency region showed a small alteration after 4000 charge-discharge cycles which indicates that the as-synthesized NWAs facilitate fast diffusion of electrolyte ions, resulting in good cycling stability. The as-prepared material bulk resistance indicated from the semi-circle in the high frequency region indicates that after 4000 and 10000 charge-discharge cycles, the bulk and charge transfer resistance start to increase leading to capacitance loss, which may be attributed to the degradation of morphology and electrolyte.

J. Chapter Summary

In this chapter, we have reported the synthesis and characterization of MnCo_2O_4 nanowire arrays as cathode materials for supercapacitor applications. MnCo_2O_4 NWAs grown over a nickel foam conductive substrate was obtained by a facile hydrothermal method with post annealing process in Air condition. The as-synthesized material was carefully characterized with XRD, XPS, SEM, TEM and BET. The electrochemical performance of the prepared cathode was investigated through CV and galvanostatic charge-discharge. The cycling perfor-

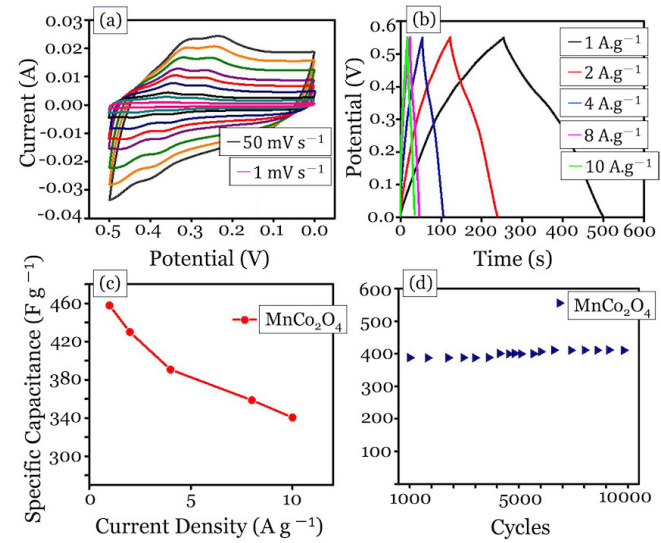


Figure 28. (a) CV curves of MnCo_2O_4 at different scanning rates, (b) galvanostatic charge/discharge curves of MnCo_2O_4 at different current densities, (c) specific capacitance at different current densities, and (d) cycling performance of MnCo_2O_4 at a current density of 1 A.g^{-1} .

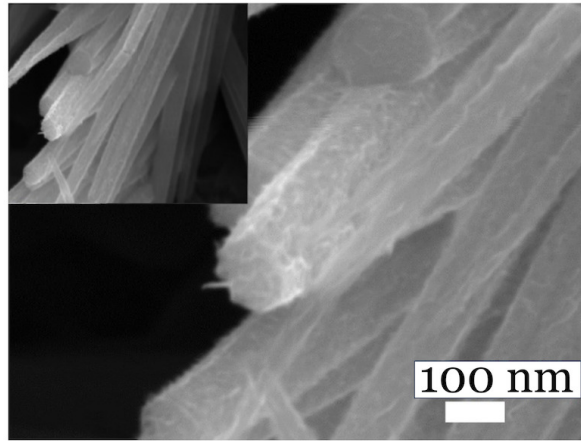


Figure 29. Typical SEM images of MnCo_2O_4 after 10000 successive cycles.

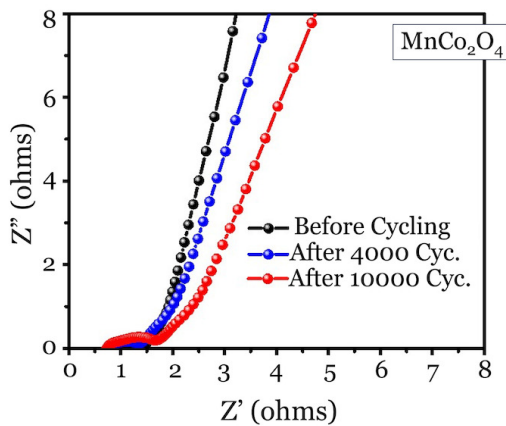


Figure 30. Electrochemical impedance spectroscopy (EIS) of MnCo_2O_4 NWAs before and after cycling.

mance has been analyzed by electrochemical impedance spectroscopy and SEM. As cathode material, MnCo_2O_4 NWAs exhibits a pseudocapacitive performance with a good capacitance of 457.85 F.g^{-1} at 1 A.g^{-1} . 74% rate capability in a $1-10 \text{ A.g}^{-1}$ current density range and 104% capacitance retention after 10000 charge/discharge cycles. Although the cycling stability was remarkably high, both the specific capacitance and rate capability need to be improved in order to meet the industrial requirements of supercapacitors. One way to achieve that is by applying unique nanostructures with well-designed architectures. Within the next chapter, we will investigate possible solutions towards this problem.

With the rapid increase of the world population and the growing crisis of global warming owing to fossil fuel consumption, intense attention is currently being paid towards exploring green and renewable energy sources to avert these aforementioned energy-related problems.[72] Electrochemical energy storage devices with emphasis on rational design at the material and device level are paving the way towards finding a worldwide solution to this energy challenge as they provide an effective implementation of the electricity generated from renewable energy sources.[73] Among the different energy storage devices, lithium-ion batteries (LIBs) are well noted for their high energy density.[3] However, they lack the higher power density, which could easily be achieved in supercapacitors ($1-10 \text{ kWkg}^{-1}$).[5] However, supercapacitors still face the problem of low energy density.[74] To increase the energy density, tremendous research efforts have been paid recently to enhancing the specific capacitance and working voltage window. In general, supercapacitors can be categorized according to the charge storage mechanism, namely electrochemical double layer capacitors (EDLCs) and pseudocapacitors. EDLCs are based on porous carbons and store charges through the physical adsorption at the electrode/electrolyte interface. On the other hand, pseudocapacitors composed mainly of transition metal oxides and conducting polymers store charges faradaically at the surface/near surface, resulting in high capacitances and energy densities compared to the carbon-based EDLCs.[75]

Due to the significant capacitances exhibited by pseudocapacitive electrodes, particularly transition metal oxides, these materials have been extensively investigated and utilized to enhance the energy densities of supercapacitors. Pseudocapacitive electrodes, such as transition metal oxides, possess high capacitances that make them attractive for improving the energy storage capabilities of supercapacitors. Extensive research efforts have been dedicated to studying and harnessing the unique properties of these materials, aiming to increase the energy densities achievable in supercapacitor devices. For instance, Chen *et al* reported an urchin-like cobalt oxide (Co_3O_4) hollow spheres for high performance supercapacitors with a high specific capacitance of 460 F.g^{-1} at a current density of 4 A.g^{-1} .[76] In recent studies, binary metal oxides such as spinel cobaltites (MCo_2O_4 ; M = Mn, Ni, Zn, Cu, etc.) have been documented to possess superior electrochemical performance over single or mono metal oxides.[52] For example, binary manganese cobaltite (MnCo_2O_4) has shown higher electrochemical activity and better electrical conductivity than unitary cobalt oxide (Co_3O_4) and manganese oxide (MnO_2). Nevertheless, MnCo_2O_4 -based electrode materials still suffer from low specific capacitance and relatively low electronic conductivity for practical supercapacitor ap-



plications. One of the effective approaches to solve this problem is to develop core-shell heterostructures by combining different pseudocapacitive and battery-type materials grown directly on conductive substrates.[77] It is well known that the 1D nanowires, nanorods and nanotubes can provide the efficient and stable pathways for electron transport and reduce the ion diffusion length when used as the core,[78] while 2D nanostructures like nanosheets and nanoflakes can ensure more electroactive sites and higher accessible surface area for ions when used as the shell.[79]

Building upon those features of 1D and 2D nanostructures, the core-shell structure holds a promising role of providing the required fast ion-electron transport pathways as well as buffering the change in volume during charge-discharge processes. Many research groups have adopted this approach and different kinds of core-shell heterostructures have been reported showing excellent electrochemical properties.[80] Metal molybdates such as NiMoO₄ and CoMoO₄ have also been widely applied in energy storage devices as battery type electrodes.[81] In specific, NiMoO₄ possesses multiple oxidation states and high redox reactivity that would result in a high battery-type specific capacitance,[82] but as a major challenge for NiMoO₄ is its poor stability for cycling that could be a result of dissolution of the active materials during cycling tests, but through the precise construction and usage of core-shell structure with nanosheets as a shell wrapping the core, it's expected to avoid the mechanical expansions and achieve a better electrochemical performance.

In this chapter, we report a binder-free heterostructure MnCo₂O₄@NiMoO₄ core-shell array grown on nickel foam substrate by a double facile hydrothermal process followed by post annealing. By exploring the synergistic effects of both components through characterization and electrochemical analysis, MnCo₂O₄@NiMoO₄ core-shell hybrid arrays demonstrated superior electrochemical performance with a specific capacitance (1244 F.g⁻¹ at 1 A.g⁻¹) and an extraordinary rate capability where 91% of capacitance retained at 10 A.g⁻¹ with a desirable life cycle (81% capacitance retention after 2500 cycles). Moreover, an asymmetric supercapacitor (ASC) was conducted based on MnCo₂O₄@NiMoO₄ core-shell NWAs and AC as the positive and negative electrode, respectively. The as-fabricated system showed a high energy density (42 W.h.kg⁻¹ at a power density of 852.3 W.kg⁻¹) as well as an excellent cycling stability with 93% retained at 8 A.g⁻¹ over 8000 cycles. Thus, the MnCo₂O₄@NiMoO₄ core-shell NWAs show great potential for supercapacitor applications.

K. Experimental Procedure

1. Synthesis of MnCo₂O₄ Hetero-Nanostructures

The reaction solution was obtained by dissolving 1 mmol Mn(NO₃)₂.4H₂O (0.25 g), 2 mmol Co(NO₃)₂.6H₂O

(0.58 g), 6 mmol NH₄F (0.22 g) and 15 mmol Urea (0.9 g) in 70 ml of distilled water with the aid of magnetic stirring for 30 min at RT. Afterwards, the resulting clear solution was transferred into a Teflon-lined stainless-steel autoclave. A pre-treated nickel foam was immersed into the reaction solution and the hydrothermal process was carried out at 120°C for 4h. After cooling down to RT, the cobalt-manganese hydroxide precursor film was removed and washed thoroughly with deionized water and ethanol absolute for several times and dried at 70°C for 12h. Finally, the precursor film was annealed at 350°C in Air for 2h and ramping rate of 1°C/min to obtain MnCo₂O₄ nanowire heterostructure array with an active mass loading of ~2 mg.cm⁻².

2. Synthesis of MnCo₂O₄@NiMoO₄ Core-Shell Hybrid Arrays

A second hydrothermal process was carried out to synthesize the MnCo₂O₄@NiMoO₄ core-shell hybrid arrays where 70 ml mixed solution of 1 mmol Na₂MoO₄.2H₂O (0.242 g) and 1 mmol Ni (No3)2.6H₂O were added to Teflon-lined stainless-steel autoclave containing Ni foam supported MnCo₂O₄ nanowire heterostructure arrays. The autoclave was maintained at 120°C for 6h. Afterwards, the autoclave was cooled down to RT, and then the sample was removed and washed thoroughly with deionized water and ethanol absolute. After drying for 12h at 70°C, the sample was annealed at 350°C for 5h in Aragon atmosphere at a ramping rate of 1°C/min. The mass loading of active material after calcination is ~5 mg/cm². For comparison, bare NiMoO₄ on Ni foam was also prepared using the same method.

3. Fabrication of an Asymmetric Supercapacitor Device

An asymmetric supercapacitor device has been prepared and tested using the synthesized MnCo₂O₄@NiMoO₄ (cathode) and activated carbon (anode). The optimal mass loadings for both electrodes were calculated using the charge balancing equation. The gravimetric energy density and power density of the hybrid full supercapacitor device were calculated using the following equations:

$$E = \frac{C \times \Delta V^2}{2 \times 3.6} \quad (13)$$

$$P = \frac{3600 \times E}{\Delta t} \quad (14)$$

Where E (W.h.kg⁻¹) is the energy density, P (W/kg⁻¹) is the power density, ΔV (V) is the potential window and Δt (s) is the discharge time.

L. $\text{MnCo}_2\text{O}_4@\text{NiMoO}_4$ Hybrid Nanowire Arrays (NWAs)

The schematic illustration shown in [Fig. 31] describes the synthesis procedure. We firstly synthesized a 3D MnCo_2O_4 heterostructure nanowire arrays directly grown on Ni foam through a facile modified hydrothermal process followed by annealing process. Then, a second hydrothermal process with post-annealing was conducted to deposit a shell of NiMoO_4 nanosheets, where the MnCo_2O_4 NWAs acted as a template for the homogeneous nucleation of the outer shell of NiMoO_4 nanosheets to finally get $\text{MnCo}_2\text{O}_4@\text{NiMoO}_4$ core-shell nanostructure. With such unique core-shell heterostructure, we could realize a better supercapacitor performance as a result of the enhanced electroactive sites and charge transfer efficiency, which are important features for faradic reactions.

1. XRD and XPS Characterization of $\text{MnCo}_2\text{O}_4@\text{NiMoO}_4$ NWAs

In order to investigate the crystal structure and chemical composition of the as synthesized material, XRD and XPS analysis were conducted using the powder scratched out of the substrate. As shown in [Fig. 32 (a)], the diffraction peaks of the core material can be well indexed with the FCC spinel structure of MnCo_2O_4 (JCPDS card no. 01-1130) and the shell correspond to diffraction peaks of NiMoO_4 (JCPDS card no. 45-0142).[83] The full scan survey spectrum of the $\text{MnCo}_2\text{O}_4@\text{NiMoO}_4$ with corresponding peaks in [Fig. 33] indicates the presence of Ni, Mo, Mn, Co and O elements. The high-resolution spectrum of Mo 3d shown in [Fig. 32 (b)] can be deconvoluted into the Mo $3d_{5/2}$ and Mo $3d_{3/2}$ of Mo^{6+} with binding energies of 232.36 and 235.5 eV, respectively.[84] [Fig. 32 (c)] shows Ni 2p the core-level spectrum with two major peaks located at 873.4 and 855.9 eV with a spin-energy separation of 17.6 eV indicating the characteristic of Ni^{2+} and corresponding to the $\text{Ni} 2p_{3/2}$ and $\text{Ni} 2p_{1/2}$ levels, respectively.[85] Lastly, the deconvolution of O 1s core-

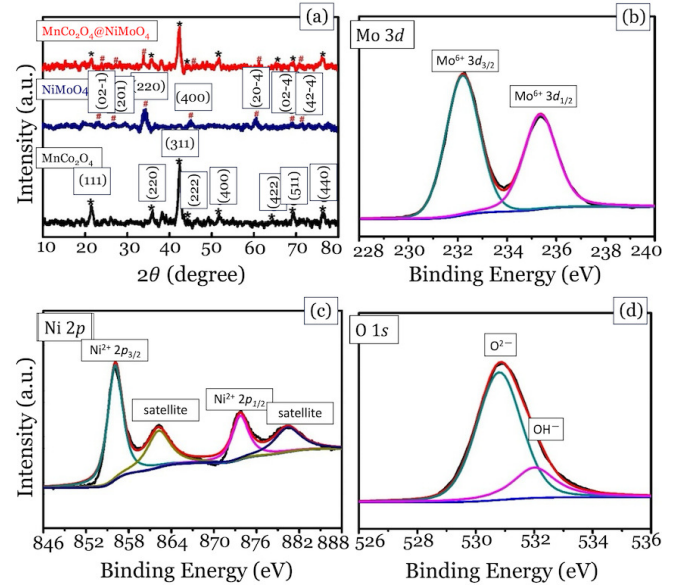


Figure 32. (a) XRD patterns of MnCo_2O_4 , NiMoO_4 and $\text{MnCo}_2\text{O}_4@\text{NiMoO}_4$ powders. (b-d) XPS survey scan of Mo 3d, Ni 2p and O 1s regions, respectively.

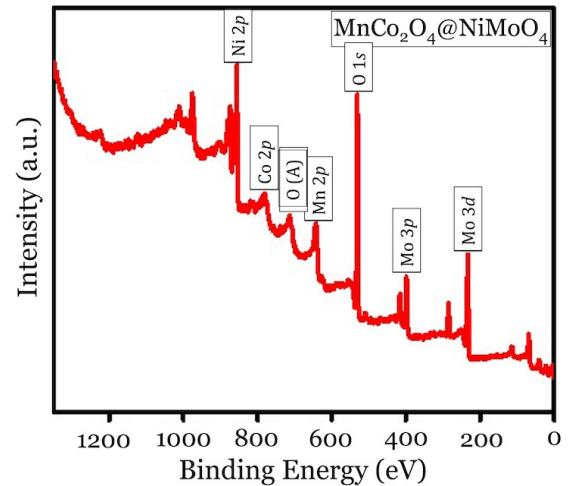


Figure 33. (a) XRD patterns of MnCo_2O_4 , NiMoO_4 and $\text{MnCo}_2\text{O}_4@\text{NiMoO}_4$ powders. (b-d) XPS survey scan of Mo 3d, Ni 2p and O 1s regions, respectively.

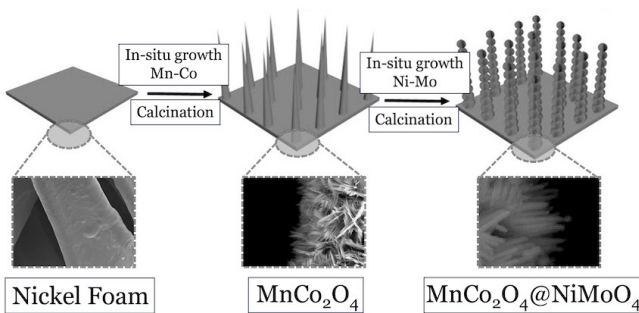


Figure 31. Schematic illustration of the fabrication process of the $\text{MnCo}_2\text{O}_4@\text{NiMoO}_4$ core-shell nanowire arrays over the nickel foam.

level spectrum in [Fig. 32 (d)] shows two peaks. The peak located at 530.8 eV is associated with the metal-oxygen bonding (oxygen binding with Mn, Co, Ni and Mo), while the other peak at 532 eV can be attributed to oxygen ions in low coordination at the surface.[69] Finally the XPS results suggest that the chemical composition of the as-prepared $\text{MnCo}_2\text{O}_4@\text{NiMoO}_4$ contains the valence of Mn (+2 and +3), Co (+2 and +3), Ni (+2) and Mo (+6) which is in good agreement with previous works.

2. Growth Mechanism of $MnCo_2O_4@NiMoO_4$ NWAs

The growth mechanism of $MnCo_2O_4@NiMoO_4$ nanowire arrays over the pre-synthesized $MnCo_2O_4$ core hybrid nanowires was studied through the morphology evolution vs time of the hydrothermal growth process. The morphology of the $NiMoO_4$ nanosheets shell was studied after 3, 6, and 12 hours. For further confirmation, the $NiMoO_4$ nanosheets were also grown directly over the nickel foam substrate in order to investigate the influence of the core nanowires on the growth orientation and to check the self-performance of the outer shell material separately. [Fig. 34] shows the growth evolution over a course of time. Choosing 6 hours as a reliable time reaction in the hydrothermal process results from the fact that a 3-hour reaction time was not enough for the $NiMoO_4$ sheets to grow as illustrated in [Fig. 34 (a)] and that over-reacting time (12 hours) would result in a dense and aggregated spherical fragments over the tips of the nanowires, which could prevent the electrolytes ions from accessing the inner core [Fig. 34 (b)].

3. Morphology Characterization of $MnCo_2O_4@NiMoO_4$ NWAs

The morphologies of $MnCo_2O_4$ NWAs and $MnCo_2O_4@NiMoO_4$ were identified by SEM as shown in [Fig. 35]. [Fig. 35 (a) and (b)] show the low and high magnification SEM images of the $MnCo_2O_4$ NWAs, respectively. As we can see with the low magnification in [Fig. 35 (a)], plenty of space could be observed in-between the nanowires, which could enhance the electrode-electrolyte interface. [Fig. 35 (b)] with a higher magnification shows that the single nanowire has an average diameter of 100 nm and an average length of 2 μm , which could increase the specific surface area and shorten the ion-diffusion pathways. Subsequently, the NWAs were used as a backbone to deposit a layer of $NiMoO_4$ to form hierarchical core-shell arrays with an average diameter of 300 nm while retaining the original length (as shown in [Fig. 35 (c) and (d)]). Such a unique and interconnected morphology could provide more open space for electrolyte access, thus more electroactive sites

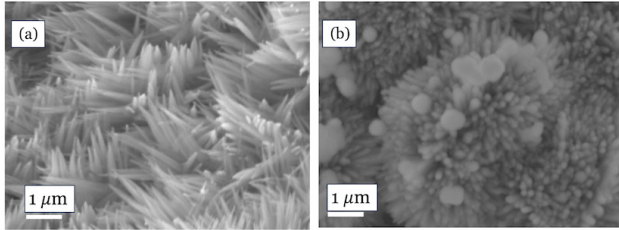


Figure 34. Typical SEM images of $MnCo_2O_4@NiMoO_4$ core-shell structure with different hydrothermal reaction duration (a) 3 hours, and (b) 12 hours, respectively.

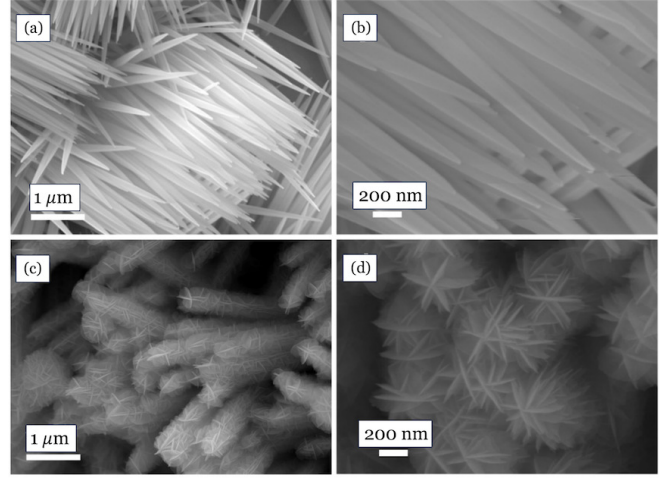


Figure 35. (a) and (b) Typical SEM images with low and high magnification of $MnCo_2O_4$ NWAs. (c) and (d) SEM images of $MnCo_2O_4@NiMoO_4$ core-shell NWAs.

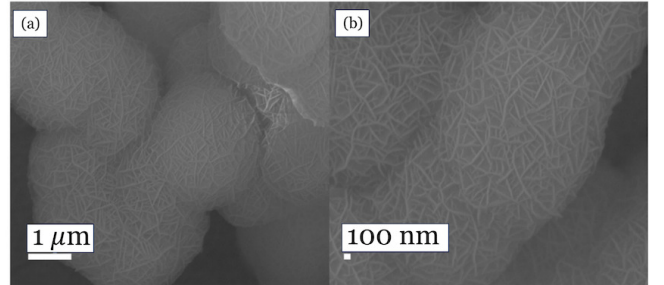


Figure 36. (a) and (b) Typical SEM images of pristine $NiMoO_4$, grown directly over the NF with high and low magnification.

for redox reactions beside the faster ion and electron transportation. For further comparison, pure $NiMoO_4$ was grown directly on Ni foam substrate as shown in [Fig. 36]. It can be observed that with the absence of the core backbone, the $NiMoO_4$ nanosheets are agglomerating onto each other to form interconnected chains of spheres with a diameter of more than 1 μm .

[Fig. 37 (a)], shows a typical TEM image that clearly indicates the existence of the hybrid core-shell structure, with ~ 100 nm $NiMoO_4$ shell in thickness coated uniformly over the core $MnCo_2O_4$ nanowires. The high-resolution TEM (HRTEM) image shown in [Fig. 37 (b)] confirm the crystalline structure of the core, where two clear lattice fringes were observed with fringe spacing of 0.47 and 0.29 nm corresponding to the (111) and (220) planes of $MnCo_2O_4$, respectively. [Fig. 37 (c)] shows the lattice fringes of the shell with fringe spacing of 0.23 and 0.24 nm corresponding to the (040) and (400) planes of $NiMoO_4$, respectively. The EDS mapping in Figure [Fig. 37 (d-i)] further confirm the distribution of elements, where Mn and Co are based within the middle area forming the core, whereas Ni and Mo are uniformly

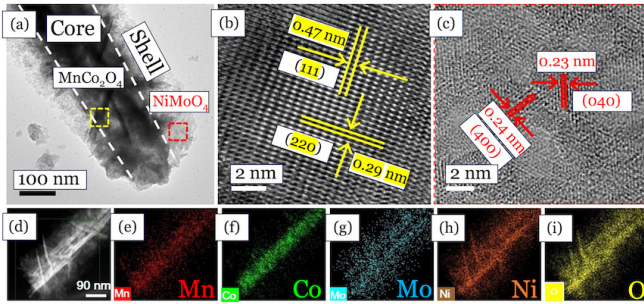


Figure 37. (a) Typical TEM of $\text{MnCo}_2\text{O}_4@\text{NiMoO}_4$ core-shell. (b,c) HRTEM of $\text{MnCo}_2\text{O}_4@\text{NiMoO}_4$ core-shell with corresponding lattice fringes, (d) hierarchical structure of $\text{MnCo}_2\text{O}_4@\text{NiMoO}_4$ core-shell with (e-i) corresponding EDS mapping.

distributed throughout the whole nanowire confirming that the hybrid is made up of MnCo_2O_4 core and coated with NiMoO_4 shell.

To further investigate the surface area and pore size distribution of the as-synthesized $\text{MnCo}_2\text{O}_4@\text{NiMoO}_4$, BET analysis have been conducted as shown in [Fig. 38 (a)]. The $\text{MnCo}_2\text{O}_4@\text{NiMoO}_4$ shows a type IV isotherm with a visible adsorbed amount at low relative pressure and a larger hysteresis loop suggesting the presence of mesopores. On the contrary, the MnCo_2O_4 has a typical type II isotherm with a very low adsorbed amount at low pressures and almost negligible desorption loop, which indicates an almost non-porous feature of the material. The estimated BET surface area of MnCo_2O_4 , NiMoO_4 ,

and $\text{MnCo}_2\text{O}_4@\text{NiMoO}_4$ where 59, 87.4 and $119.2 \text{ m}^2/\text{g}$ respectively, implying that the core-shell heterostructure possesses a larger surface area which could be an indicator for better electrochemical performance. With regard to the pore size distribution [Fig. 38 (b)], the pore sizes of the core-shell heterostructure are distributed nearby 8.5 nm, which is a suitable size for diffusion of active species inside the electrode material.

4. Electrochemical Characterization of $\text{MnCo}_2\text{O}_4@\text{NiMoO}_4$ NWAs

In order to evaluate the validity of the fabricated material for supercapacitor applications, MnCo_2O_4 , NiMoO_4 , and $\text{MnCo}_2\text{O}_4@\text{NiMoO}_4$ were tested separately as working electrodes using three-electrode cell system with the as-synthesized materials as the working electrode, SCE as reference electrode and Pt plate as counter-electrode in a 1 M KOH electrolyte. [Fig. 39 (a)] displays the CV curves of the as-synthesized materials in a potential window of 0–0.6 V and at a scan rate of 1 mV.s^{-1} . It is noteworthy that the CV curve of the $\text{MnCo}_2\text{O}_4@\text{NiMoO}_4$ shows the largest integrated area with the highest peak current as well, indicating a larger specific capacitance than both pristine MnCo_2O_4 (core) and NiMoO_4 (shell). It is also obvious that all obtained electrodes show a pair of redox peaks, which denotes a signature of faradic behavior. [Fig. 40 (a)], shows the CV curves of $\text{MnCo}_2\text{O}_4@\text{NiMoO}_4$ core-shell NWAs in a potential window from 0 to 0.6 V at different scan rates ranging from 1 to 50 mV.s^{-1} . At lower scanning rates, a pair of redox peaks are noticeable indicating the existence of faradic processes, which could

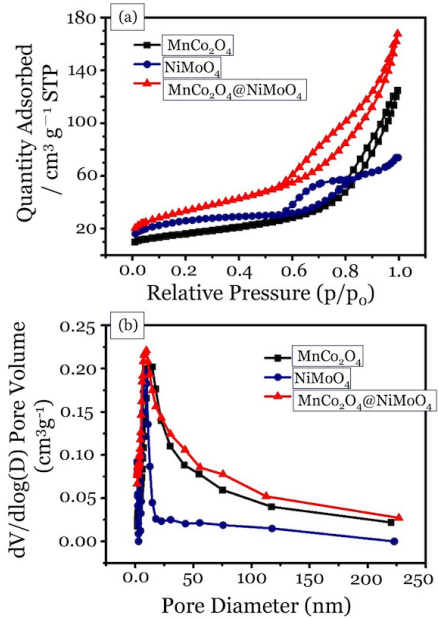


Figure 38. (a) N_2 adsorption-desorption isotherms and (b) corresponding pore size distribution curves of MnCo_2O_4 , NiMoO_4 , and $\text{MnCo}_2\text{O}_4@\text{NiMoO}_4$.

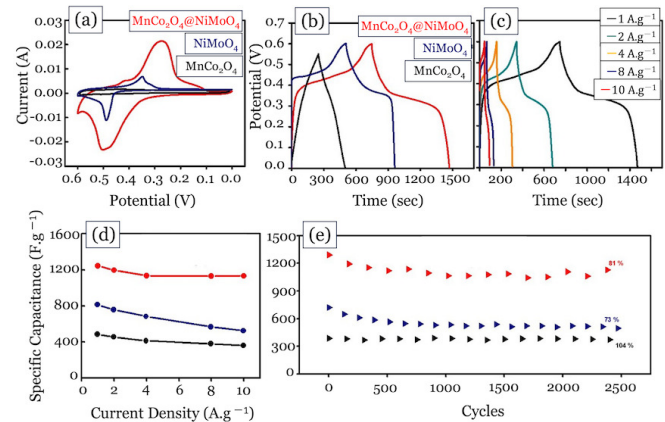


Figure 39. (a) CV curves obtained at a scan rate of 1 mV.s^{-1} and (b) Galvanostatic charge-discharge curves obtained at a current density of 1 A.g^{-1} of MnCo_2O_4 , NiMoO_4 , and $\text{MnCo}_2\text{O}_4@\text{NiMoO}_4$ electrodes. (c) Galvanostatic charge-discharge curves obtained at different current densities of $\text{MnCo}_2\text{O}_4@\text{NiMoO}_4$ electrode. (d) Specific Capacitance at different current densities, and (e) Cycling performance of MnCo_2O_4 , NiMoO_4 , and $\text{MnCo}_2\text{O}_4@\text{NiMoO}_4$ at a current density of 5 A.g^{-1} .

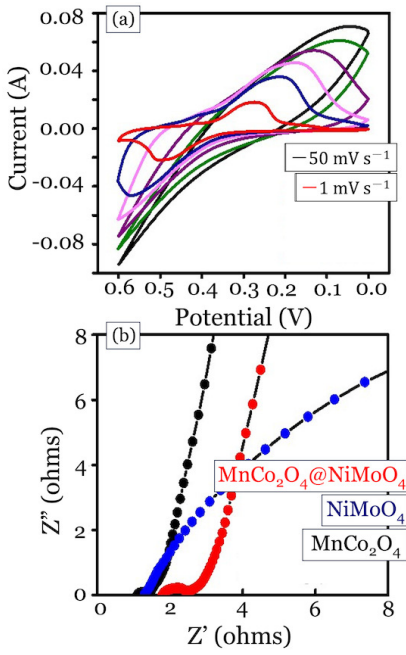


Figure 40. (a) CV curves of MnCo₂O₄@NiMoO₄ obtained at different scanning rates, (b) EIS measurements of MnCo₂O₄, NiMoO₄, and MnCo₂O₄@NiMoO₄ electrodes.

be an attribution of reversible conversion of Mn²⁺/Mn⁺, Co⁴⁺/Co³⁺, and Ni³⁺/Ni²⁺.[63] We can observe that the electrode is showing a capacitive behavior as the current peak is increased gradually with the increment of scanning rate. However, oxidation and reduction peaks start to shift to the anodic and cathodic directions respectively at larger scanning rates and that is because of more substantial polarization.[86]

For further comparison, the GCD curves of the MnCo₂O₄, NiMoO₄, and MnCo₂O₄@NiMoO₄ were studied as well at the same current density of 1 A.g⁻¹ [Fig. 39 (b)]. It is clearly seen that the MnCo₂O₄@NiMoO₄ core-shell heterostructure demonstrates a longer discharge time and for that matter, a higher specific capacitance than unitary materials of MnCo₂O₄ and NiMoO₄. This increased capacitance observed in the core-shell structure can be attributed to the synergistic effects of the structure composition. [Fig. 39 (c)] exhibits the GCD curves of the MnCo₂O₄@NiMoO₄ core-shell NWAs within the potential window of 0–0.6 V at different current densities ranging 1–10 A.g⁻¹. It can be seen that there is a large plateau within the discharge curves, which could explain the dominant faradic behavior of the as-fabricated electrode compared with the pristine MnCo₂O₄. We can also observe the approximate symmetry between charge and discharge curves, which also indicates the superior electrochemical behavior.

The specific capacitances of the as-fabricated materials MnCo₂O₄, NiMoO₄, and MnCo₂O₄@NiMoO₄ have been determined and calculated using the galvanostatic charge-discharge data as shown in [Fig. 39 (d)]. As ex-

pected, the core-shell MnCo₂O₄@NiMoO₄ NWAs delivered the highest specific capacitance and impressively highest rate capability. The specific capacitance was 1244, 1195, 1133, 1130 and 1132 F.g⁻¹ at current densities of 1, 2, 4, 8 and 10 A.g⁻¹, respectively. The specific capacitance of MnCo₂O₄@NiMoO₄ electrode was 1244 F.g⁻¹ at 1 A.g⁻¹, which is much way higher than that of pristine MnCo₂O₄ (457.85 F.g⁻¹) and NiMoO₄ (762.5 F.g⁻¹) at the same current density. Not only the specific capacitance, but also the rate capability was also increased in such an efficient way as we increased the current density from 1 to 10 A.g⁻¹, about 91% of MnCo₂O₄@NiMoO₄ initial capacitance has been retained compared with its other counterparts MnCo₂O₄ and NiMoO₄ only 74% and 64% has been retained at the same current range, respectively. The higher capacitance and the better rate capability could be attributed to various reasons. Firstly, the core heterostructure MnCo₂O₄ NWAs has a high crystallinity and it is grown directly and tightly over the nickel foam current collector, which can provide a fast electron transport. Secondly, the high surface area of the 3D porous nanostructure core-shell architecture, coming directly from the mesoporous nature of the outer shell, can provide fast ion diffusion and intimate the electrode/electrolyte contact. Thirdly, the Synergistic effects between the chemical composition of both core and shell structures.[87] Table II compares the specific capacitance of the prepared mixed metal oxides core-shell structure with previously reported studies, where we can find that the specific capacitance of our prepared MnCo₂O₄@NiMoO₄ is competitive to the summarized electrodes.

The EIS measurements shown in [Fig. 40 (b)], reveals that the core MnCo₂O₄ with a mass loading of ~2 mg/cm² is showing the largest slope in low-frequency region and the smallest charge transfer resistance (R_{ct}) estimated from the semicircle in high-frequency region. It is obvious that the relatively larger resistance within the core-shell structure is coming from the higher mass loading of active material per meter square in the case of MnCo₂O₄@NiMoO₄ where the high mass loading (~5 mg/cm²) adds more thickness to the electrode and makes it harder for ions to reach the lower levels. However, the core-shell structure still shows a better capacitive characteristics and electrochemical performance and that is because it has more active sites and higher surface area for reactions than the core. The cycling ability of the prepared electrodes was determined by conducting successive charge-discharge tests at a current density of 5 A.g⁻¹ for 2500 cycles. [Fig. 39 (e)], shows that MnCo₂O₄@NiMoO₄ still delivers a high capacitance after 2500 cycles retaining 81% of its initial capacitance, indicating a good cycling stability at a current density of 5 A.g⁻¹. The degradation of cycling stability of core-shell could be a result of the destruction of the NiMoO₄ shell, which was showing a lower retention than the other counterparts as it is shown in [Fig. 39 (e)], which may cause a blockage between the core and the ion elec-

Table II. Specific capacitance comparison of current work against previously reported electronde materials.

Electrode Material	Electrolyte	Specific Capacitance
MnCo ₂ O ₄ Nanowire arrays	1 M KOH	349.0 F.g ⁻¹ @ 1.0 A.g ⁻¹ [59]
MnCo ₂ O ₄ Nanosheet films	—	400.0 F.g ⁻¹ @ 1.0 A.g ⁻¹ [88]
Urchin like MnCo ₂ O _{4.5}	—	129.2 F.g ⁻¹ @ 0.1 A.g ⁻¹ [89]
MnCo ₂ O _{4.5} Nanosheets	6 M KOH	420.0 F.g ⁻¹ @ 1.0 A.g ⁻¹ [90]
MnCo ₂ O ₄ @Ni(OH) ₂ hierarchical structure	2 M KOH	2154 F.g ⁻¹ @ 5.0 A.g ⁻¹ [83]
MnCo ₂ O ₄ @MnO ₂ hierarchical structure	3 M KOH	858.0 F.g ⁻¹ @ 1.0 A.g ⁻¹ [62]
MnO ₂ @NiMoO ₄ core-shell hierarchical structure	2 M KOH	582.2 F.g ⁻¹ @ 1.0 A.g ⁻¹ [67]
Nanosheet-based CoMoO ₄ -NiMoO ₄ nanotubes	3 M KOH	751.0 F.g ⁻¹ @ 1.0 A.g ⁻¹ [91]
NiCo ₂ O ₄ -rGO composite	2 M KOH	1222 F.g ⁻¹ @ 0.5 A.g ⁻¹ [92]
This Work	1 M KOH	1244 F.g ⁻¹ @ 1.0 A.g ⁻¹ [93]

troytes. By comparing the morphologies of MnCo₂O₄ and MnCo₂O₄@NiMoO₄ after cycling (see [Fig. 41]), it has been shown that the pristine nanowires were more preserved than the core-shell electrode after cycling and that the destroyed outer shell may be blocking the electrolyte ions from accessing the inner nanowire cores.

5. Electrochemical Characterization of pristine-NiMoO₄ Nanosheets

To study the electrochemical performance of pristine-NiMoO₄ Nanosheets grown directly over the 3D nickel foam substrate, CV and GCD tests were carried out in a three-electrode system with a Pt plate as a counter electrode and a saturated calomel electrode as reference electrode in 2 M KOH electrolyte. [Fig. 42 (a)] shows the CV curves of NiMoO₄ at different scan rates from 1 to 20 mV.s⁻¹ tested in a 0–0.6 V potential range. The

charge storage mechanism in NiMoO₄ can be ascribed to pseudocapacitance as deduced from the shape of the CV curves. The curves show a pair of anodic and cathodic peaks arising from fast faradic redox reactions of Ni(II) ⇌ Ni(III) during charge and discharge. The NiMoO₄ nanosheets exhibit good electrochemical reversibility as evidenced by the near mirror symmetry of both anodic and cathodic peaks. The GCD curves of the NiMoO₄ nanosheets are shown in [Fig. 42 (b)]. The specific capacitance is calculated from this curve. As shown in [Fig. 42 (c)], the NiMoO₄ electrode delivers a high capacitance of 762.5 F.g⁻¹ and a rate capability of 64% in a current range of 1–10 A.g⁻¹. The as-prepared pure NiMoO₄ electrode shows a reasonable cycling performance, 73% of capacitance retention after 2500 charge-discharge cycles. The limited cycling life could be a result of the degradation of the morphology and electrolyte.

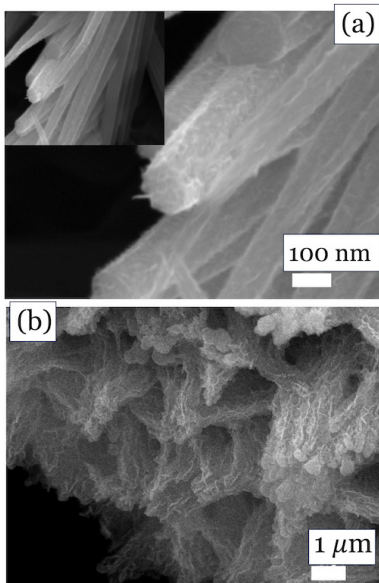


Figure 41. (a) Typical SEM images of MnCo₂O₄ after cycling (b) MnCo₂O₄@NiMoO₄ SEM images after cycling.

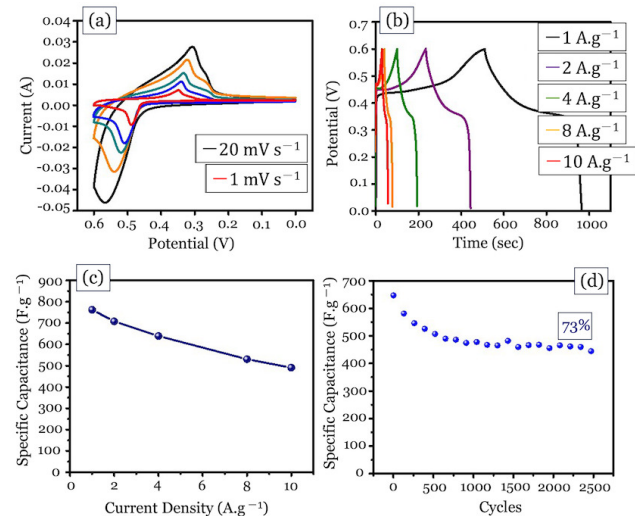


Figure 42. (a) CV curves obtained at different scan rates up to 20 mV.s⁻¹ NiMoO₄ and (b) GCD curves obtained at different current densities of NiMoO₄ (c) specific capacitance of NiMoO₄ electrode at different current densities and (d) cycling stability of NiMoO₄ after over 2500 charge-discharge cycles.

6. $MnCo_2O_4@NiMoO_4//AC$ Asymmetric Supercapacitor

Asymmetric supercapacitors, a type of hybrid capacitors assembled by two dissimilar electrode materials offer a distinct advantage of wide potential voltage window, and thereby significantly enhance the energy density. Looking back to the main goal that we seek in developing supercapacitors, which is enhancing the energy density, the fundamental principles behind batteries and supercapacitors could come together to achieve that goal. The battery-type electrode (cathode) will represent the energy source, whilst the capacitor-type electrode (anode) will represent the power source. Typically, in a symmetric supercapacitor, the working voltage is limited to less than 1.0 V because of the thermodynamic breakdown potential of water molecules when aqueous electrolytes are used. Nevertheless, the working voltage can be improved beyond 2.5 V by using organic electrolytes. However, these organic electrolytes are sometimes toxic and environmentally benign for certain applications. Therefore, a feasible approach to achieve higher working voltage for aqueous electrolytes is to use two different electrode materials for the anode and the cathode.

To further evaluate the practical application of $MnCo_2O_4@NiMoO_4$ core-shell structure, an asymmetric supercapacitor device (ASC) has been prepared, where we used the as-prepared $MnCo_2O_4@NiMoO_4$ as a positive electrode and activated carbon (AC) as the negative electrode in 1 M KOH. The electrochemical performance of the supercapacitor device was characterized by CV at different scanning rates and GCD measurements at various current densities. The mass loading of both electrodes was determined using the charge balance equation, where we used 10 mg/cm² of active carbon. The electrochemical performance of AC is shown in [Fig. 43] with a semi-rectangular CV and symmetric charge-discharge curve.

The specific capacitance of the negative electrode at 1 A.g⁻¹ was 270 F.g⁻¹. [Fig. 44 (a)], shows the CV curves of $MnCo_2O_4@NiMoO_4//AC$ full device within a potential window of 0 to 1.6 V at different scanning rates. [Fig. 44 (b)], shows the GCD tests at different current densities. For the relation between

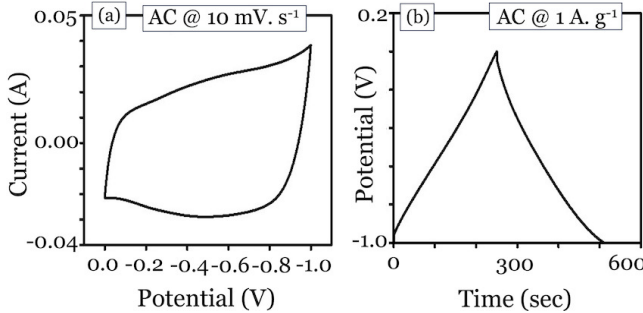


Figure 43. (a) CV curve of AC at a scanning rate of 10 mV.s^{-1} . (b) GCD of AC at a current density of 1 A.g^{-1} .

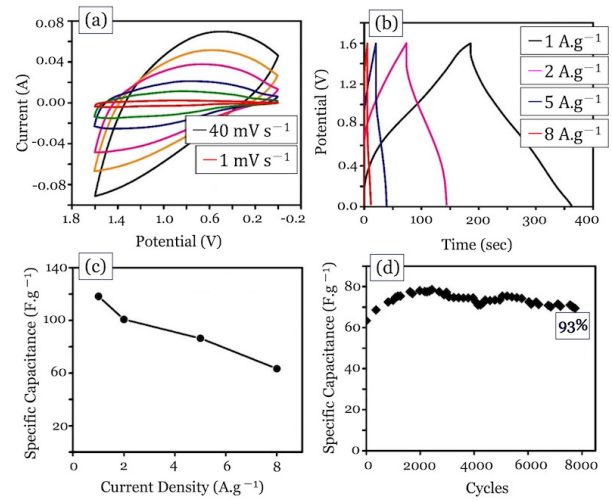


Figure 44. (a) CV and (b) GCD curves of the $MnCo_2O_4@NiMoO_4//AC$ device with various scanning rates and current densities. (c) Specific capacitance of the $MnCo_2O_4@NiMoO_4//AC$ device at various current densities. (d) Cycling performance of the $MnCo_2O_4@NiMoO_4//AC$ device at a current density of 8 A.g^{-1} .

specific capacitance and current density, it has been shown in [Fig. 44 (c)]. The specific capacitance of the full device is up to 118.27 F.g^{-1} at 1 A.g^{-1} . About 93% of this capacitance has been retained after 8000 cycles at a current density of 8 A.g^{-1} as it is shown in [Fig. 44 (d)]. It is noteworthy that the ASC device exhibited a high energy density of 42 W.h.kg^{-1} at a power density of 852.3 W.kg^{-1} (see [Fig. 45] for the Ragone plot), which is comparable with previously reported studies such as $\text{CoMoO}_4@NiMoO_4$ ($28.78 \text{ W.h.kg}^{-1}$),[82] $\text{NiCo}_2\text{O}_4@MnO_2$ (35 W.h.kg^{-1}),[94] $\text{MnCo}_2\text{O}_4@Ni(\text{OH})_2$ (48 W.h.kg^{-1}),[83] $\text{MnO}_2@NiMoO_4$ (32.5 W.h.kg^{-1})[95] and $\text{NiCo}_2\text{S}_4@NiMoO_4$ (21.4 W.h.kg^{-1}).[68]

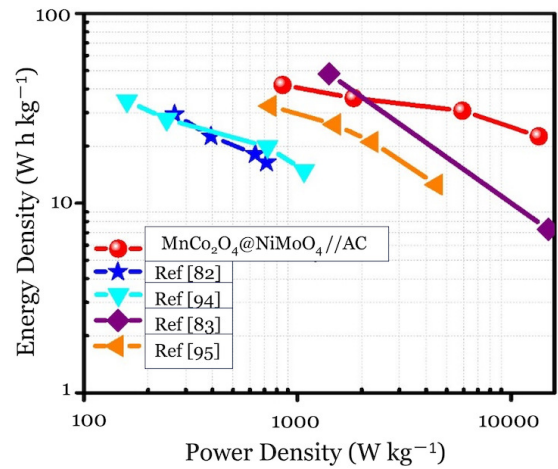


Figure 45. Ragone plot of $MnCo_2O_4@NiMoO_4//AC$ device.

M. Chapter Summary

In this chapter, the hierarchical $\text{MnCo}_2\text{O}_4@\text{NiMoO}_4$ core-shell NWAs were prepared through conventional hydrothermal and annealing procedures without any binders. When evaluated as a cathode for supercapacitors, the hierarchical $\text{MnCo}_2\text{O}_4@\text{NiMoO}_4$ core-shell NWAs show an improved specific capacitance of 1244 F.g^{-1} at 1 A.g^{-1} and extraordinary capacitance preservation, where 91% of the starting capacitance was conserved at 10 A.g^{-1} .

The electrochemical analysis and characterization disclosed that the superior performance could be attributed to the interactive effect between the chemical composition of both core and shell structures and the high surface area of the 3D porous nanostructure coming directly from the mesoporous nature of the outer shell, which could provide a larger contact area between electrolyte and electrode surfaces with a fast diffusion of ions.

The validation of the as-synthesized electrode material for real applications has been proved by applying a full cell asymmetric supercapacitor device where $\text{MnCo}_2\text{O}_4@\text{NiMoO}_4$ and AC act as a cathode and an anode, respectively. $\text{MnCo}_2\text{O}_4@\text{NiMoO}_4//\text{AC}$ has a high energy density of 42 W.h.kg^{-1} with a power density of 852.3 W.kg^{-1} , which is better than those of previously reported similar studies, and a reliable cycling capability where 93% of initial capacitance was conserved after 8000 cycles. These good electrochemical performances open up the possibility for further applications of the $\text{MnCo}_2\text{O}_4@\text{NiMoO}_4$ NWA material within the practical applications of energy storage devices.

Chapter V: Conclusion and Prospective of Future Work

Despite the fact that a lot of research has been deployed on replacing EDLC electrodes in supercapacitors with pseudocapacitive electrode materials, the commercial application of those developments and researches needs to be further optimized before putting it into industry. The main factor comes from the fact that pseudocapacitive materials like metal oxides and polymers still lack the proper electronic conductivity and cycle life to meet the required specification of effective energy storage devices. In this study, we have proposed that by applying a well-designed macro-nano structures of binary metal oxides like core-shell structures with unique and novel morphology, the specific capacitance and rate capability of the pseudocapacitive material will be enhanced, making benefits of higher electron conductivity and short path ways within this architecture. We chose manganese cobalt oxide as a cathode material for supercapacitors, synthesized directly as hybrid arrays of nanowires over a substrate of nickel foam without any binders because of the low cost, environmental benignity, and high theoretical capacitance of the binary oxide over the monoxide.

Moreover, nickel molybdate oxide was chosen to be grown over the previous nanowire array of manganese cobalt oxide with a novel and rationally-designed nanosheets. A design that showed better performance in terms of high specific capacitance and rate capability.

In summary, the core-shell $\text{MnCo}_2\text{O}_4@\text{NiMoO}_4$ NWAs have been successfully fabricated over a nickel foam substrate through a facile two-step hydrothermal method and without any binders. We carefully characterized the individual electrodes by XRD, XPS, SEM, TEM, BET and CV techniques before fabricating a full asymmetric supercapacitor device with $\text{MnCo}_2\text{O}_4@\text{NiMoO}_4$ as a cathode and active carbon as an anode. We arrived at the following conclusions at the end of the study.

1. The hierarchical $\text{MnCo}_2\text{O}_4@\text{NiMoO}_4$ core-shell nanowire arrays are synthesized *via* facile and conventional two-step hydrothermal method with post-annealing, which display enhanced electrochemical performance, especially high-rate capability and specific capacitance.
2. When evaluated as a cathode for supercapacitors, the hierarchical $\text{MnCo}_2\text{O}_4@\text{NiMoO}_4$ core-shell nanowire arrays show a high specific capacitance of 1244 F.g^{-1} at 1 A.g^{-1} , and an extraordinary rate capability of 91% capacitance retained at a current density of 10 A.g^{-1} .
3. By using the proper characterizations and electrochemical analysis, we disclosed that the superior performance could be attributed to the synergistic effect between the chemical composition of both core and shell structures, as well as the high surface area of the 3D porous nanostructure coming directly from the mesoporous nature of the outer shell, which could provide fast ion diffusion and intimate the electrode/electrolyte contact.
4. The validation of as-synthesized electrode material for real applications has been proved by fabricating an asymmetric supercapacitor using $\text{MnCo}_2\text{O}_4@\text{NiMoO}_4$ as a cathode and active carbon as an anode. The $\text{MnCo}_2\text{O}_4@\text{NiMoO}_4//\text{AC}$ has high energy density of 42 W.h.kg^{-1} at a power density of 852.3 W.kg^{-1} , which is better than previously reported works and a good cycling stability with 93% capacitance retention after 8000 cycles.

N. Future Perspectives

Compared with other energy storage devices, supercapacitors have superior qualities, including a long cycle life, fast charge/discharge processes, and a high safety rating. The practical use of supercapacitor devices is hindered by their low energy density. The possible pathways for enhancing the energy density *via* improving capacitance and working voltage are of key factors on this

path. Choosing the right electrode material whether as a cathode or anode should take into consideration an optimal design perspective.

We suggest that future research should be directed towards:

1. full exploration of novel types of electrodes and electrolyte materials regardless of the supercapacitor type. To achieve that, various experimental and computational investigations are required, such as theory, modeling, and simulations. Such computational research can direct the design options for electrode and electrolyte materials.

2. Future work should focus on increasing the capacitance and working voltage through enhancing the effective surface area, optimizing the pore size and volume, and providing surface functional groups to increase the pseudocapacitance contribution.

3. Integrating various capacitive materials with rational nanostructures should be further studied in order to get an in-depth understanding of the synergistic effects between the chemical components.

-
- [1] R. Dronskowski, S. Kikkawa, and A. Stein, *Handbook of Solid State Chemistry* (Wiley-VCH Verlag GmbH & Co. KGaA, Weinheim, Germany, 2017).
- [2] W. Pell and B. Conway, Quantitative modeling of factors determining ragone plots for batteries and electrochemical capacitors, *J. Power Sources* **63**, 255 (1996).
- [3] Y. Gogotsi and R. M. Penner, Energy storage in nanomaterials – capacitive, pseudocapacitive, or battery-like?, *ACS Nano* **12**, 2081 (2018).
- [4] P. Simon and Y. Gogotsi, Materials for electrochemical capacitors, *Nat. Mater* **7**, 845 (2008).
- [5] G. Wang, L. Zhang, and J. Zhang, A review of electrode materials for electrochemical supercapacitors, *Chem. Soc. Rev.* **41**, 797 (2012).
- [6] A. Du Pasquier, I. Plitz, S. Menocal, and G. Amatucci, A comparative study of li-ion battery, supercapacitor and nonaqueous asymmetric hybrid devices for automotive applications, *J. Power Sources* **115**, 171 (2003).
- [7] A. González, E. Goikolea, J. A. Barrena, and R. Mysyk, Review on supercapacitors: Technologies and materials, *Renew. Sustain. Energy Rev.* **58**, 1189 (2016).
- [8] A. Pandolfo and A. Hollenkamp, Carbon properties and their role in supercapacitors, *J. Power Sources* **157**, 11 (2006).
- [9] Y. Pleskov, *Fundamentals of electrochemistry (2nd edition)*, Vol. 43 (2007) pp. 1326–1327.
- [10] L. L. Zhang and X. S. Zhao, Carbon-based materials as supercapacitor electrodes, *Chem. Soc. Rev.* **38**, 2520 (2009).
- [11] P. Sharma and T. Bhatti, A review on electrochemical double-layer capacitors, *Energy Convers. Manag.* **51**, 2901 (2010).
- [12] Capacitance limits of high surface area activated carbons for double layer capacitors, *Carbon* **43**, 1303 (2005).
- [13] D. Qu and H. Shi, Studies of activated carbons used in double-layer capacitors, *J. Power Sources* **74**, 99 (1998).
- [14] J. Gamby, P. Taberna, P. Simon, J. Fauvarque, and M. Chesneau, Studies and characterisations of various activated carbons used for carbon/carbon supercapacitors, *J. Power Sources* **101**, 109 (2001).
- [15] H. Shi, Activated carbons and double layer capacitance, *Electrochim. Acta* **41**, 1633 (1996).
- [16] Y. Zhu *et al.*, Carbon-based supercapacitors produced by activation of graphene, *Science* **332**, 1537 (2011).
- [17] Z. Fan, J. Yan, T. Wei, L. Zhi, G. Ning, T. Li, and F. Wei, Asymmetric supercapacitors based on Graphene/MnO₂ and activated carbon nanofiber electrodes with high power and energy density, *Adv. Funct. Mater.* **21**, 2366 (2011).
- [18] D. Hulicova-Jurcakova, M. Seredych, G. Q. Lu, and T. J. Bandosz, Combined effect of nitrogen- and oxygen-containing functional groups of microporous activated carbon on its electrochemical performance in supercapacitors, *Adv. Funct. Mater.* **19**, 438 (2009).
- [19] M. Mastragostino, C. Arbizzani, L. Meneghelli, and R. Paraventi, Electronically conducting polymers and activated carbon: Electrode materials in supercapacitor technology, *Adv. Mater.* **8**, 331 (1996).
- [20] V. Ruiz, C. Blanco, R. Santamaría, J. Ramos-Fernández, M. Martínez-Escandell, A. Sepúlveda-Escribano, and F. Rodríguez-Reinoso, An activated carbon monolith as an electrode material for supercapacitors, *Carbon* **47**, 195 (2009).
- [21] H. Liu, P. He, Z. Li, Y. Liu, and J. Li, A novel nickel-based mixed rare-earth oxide/activated carbon supercapacitor using room temperature ionic liquid electrolyte, *Electrochim. Acta* **51**, 1925 (2006).
- [22] K. H. An, W. S. Kim, Y. S. Park, J.-M. Moon, D. J. Bae, S. C. Lim, Y. S. Lee, and Y. H. Lee, Electrochemical properties of high-power supercapacitors using single-walled carbon nanotube electrodes, *Adv. Funct. Mater.* **11**, 387 (2001).
- [23] Z. Fan *et al.*, A three-dimensional carbon nanotube/graphene sandwich and its application as electrode in supercapacitors, *Adv. Mat.* **22**, 3723 (2010).
- [24] D. N. Futaba *et al.*, Shape-engineerable and highly densely packed single-walled carbon nanotubes and their application as super-capacitor electrodes, *Nat. Mat.* **5**, 987 (2006).
- [25] C. Liu, Z. Yu, D. Neff, A. Zhamu, and B. Z. Jang, Graphene-based supercapacitor with an ultrahigh energy density, *Nano Letters* **10**, 4863 (2010).
- [26] Y. Zhao *et al.*, Highly compression-tolerant supercapacitor based on polypyrrole-mediated graphene foam electrodes, *Adv. Mat.* **25**, 591 (2013).
- [27] Z. Wen *et al.*, Crumpled nitrogen-doped graphene nanosheets with ultrahigh pore volume for high-performance supercapacitor, *Adv. Mat.* **24**, 5610 (2012).
- [28] T. Wigmans, Industrial aspects of production and use of activated carbons, *Carbon* **27**, 13 (1989).
- [29] A. Jänes, H. Kurig, and E. Lust, Characterisation of activated nanoporous carbon for supercapacitor electrode

- materials, *Carbon* **45**, 1226 (2007).
- [30] M. Lillo-Ródenas, D. Cazorla-Amorós, and A. Linares-Solano, Understanding chemical reactions between carbons and NaOH and KOH: An insight into the chemical activation mechanism, *Carbon* **41**, 267 (2003).
- [31] K. Kierzek, E. Frackowiak, G. Lota, G. Gryglewicz, and J. Machnikowski, Electrochemical capacitors based on highly porous carbons prepared by KOH activation, *Electrochim. Acta* **49**, 515 (2004).
- [32] M. Zhi, F. Yang, F. Meng, M. Li, A. Manivannan, and N. Wu, Effects of pore structure on performance of an activated-carbon supercapacitor electrode recycled from scrap waste tires, *ACS Sustainable Chem. Eng.* **2**, 1592 (2014).
- [33] L. Li, Z. Hu, N. An, Y. Yang, Z. Li, and H. Wu, Facile synthesis of MnO₂/CNTs composite for supercapacitor electrodes with long cycle stability, *J. Phys. Chem. C* **118**, 22865 (2014).
- [34] Z. Chen *et al.*, High-performance supercapacitors based on intertwined CNT/V₂O₅ nanowire nanocomposites, *Adv. Mat.* **23**, 791 (2011).
- [35] K. Novoselov, A. Geim, S. Morozov, D. Jiang, Y. Zhang, S. Dubonos, I. Grigorieva, and A. Firsov, Electric field effect in atomically thin carbon films, *Nat. Mater.* **6**, 666 (2004).
- [36] L. Le, M. Ervin, H. Qiu, B. Fuchs, and W. Lee, Graphene supercapacitor electrodes fabricated by inkjet printing and thermal reduction of graphene oxide, *Electrochem. commun.* **13**, 355 (2011).
- [37] K. Lota, V. Khomenko, and E. Frackowiak, Capacitance properties of poly(3,4-ethylenedioxythiophene)/carbon nanotubes composites, *J. Phys. Chem. Solids* **65**, 295 (2004).
- [38] R. M. Bandeira, D. D. da Silva, M. Khalid, and G. Tremiliosi-Filho, Synthesis of polyaniline/5-sulfosalicylic acid composite and its electrochemical properties, *Mater. Sci. Energy Technol.* **3**, 487 (2020).
- [39] L. Wei, M. Sevilla, A. B. Fuertes, R. Mokaya, and G. Yushin, Polypyrrole-derived activated carbons for high-performance electrical double-layer capacitors with ionic liquid electrolyte, *Adv. Funct. Mater.* **22**, 827 (2012).
- [40] K. Liu, Z. Hu, R. Xue, J. Zhang, and J. Zhu, Electropolymerization of high stable poly (3, 4-ethylenedioxythiophene) in ionic liquids and its potential applications in electrochemical capacitor, *J. Power Sources* **179**, 858 (2008).
- [41] A. Laforgue, P. Simon, C. Sarrazin, and J.-F. Fauvarque, Polythiophene-based supercapacitors, *J. Power Sources* **80**, 142 (1999).
- [42] M. Zhong, Y. Li, C. Ma, X. Zhai, J. Shi, Q. Guo, and L. Liu, Effect of reduced graphene oxide on the properties of an activated carbon cloth/polyaniline flexible electrode for supercapacitor application, *J. Power Sources* **217**, 6–12 (2012).
- [43] J. Long, K. Swider, C. Merzbacher, and D. Rolison, Voltammetric characterization of ruthenium oxide-based aerogels and other RuO₂ solids: The nature of capacitance in nanostructured materials, *Langmuir* **19**, 2532 (2003).
- [44] M. Toupin, T. Brousse, and D. Bélanger, Charge storage mechanism of MnO₂ electrode used in aqueous electrochemical capacitor, *Chem. Mater.* **16**, 3184–3190 (2004).
- [45] Y. Wang, Y. Lei, J. Li, L. Gu, H. Yuan, and D. Xiao, Synthesis of 3D-nanonet hollow structured Co₃O₄ for high capacity supercapacitor, *ACS Appl. Mater. Interfaces* **6**, 6739–6747 (2014).
- [46] P. Rodgers and J. Heath, *Nanoscience and Technology: A Collection of Reviews from Nature Journals* (2009) pp. 1–346.
- [47] V. Patake, S. Pawar, V. Shinde, T. Gujar, and C. Lokhande, The growth mechanism and supercapacitor study of anodically deposited amorphous ruthenium oxide films, *Curr. Appl. Phys.* **10**, 99 (2010).
- [48] S. Pang and M. Anderson, Novel electrode materials for electrochemical capacitors: Part II. Material characterization of sol-gel-derived and electrodeposited manganese dioxide thin films, *J. Mater. Res.* **15**, 2096 (2000).
- [49] J. W. Lee, A. S. Hall, J.-D. Kim, and T. E. Mallouk, A facile and template-free hydrothermal synthesis of Mn₃O₄ nanorods on graphene sheets for supercapacitor electrodes with long cycle stability, *Chem. Mater.* **24**, 1158 (2012).
- [50] S.-Y. Wang, K.-C. Ho, S.-L. Kuo, and N.-L. Wu, Investigation on capacitance mechanisms of Fe₃O₄ electrochemical capacitors, *J. Electrochem. Soc.* **153**, A75 (2006).
- [51] C. Yuan *et al.*, Template-engaged synthesis of uniform mesoporous hollow NiCo₂O₄ sub-microspheres towards high-performance electrochemical capacitors, *RSC Advances* **3**, 18573 (2013).
- [52] Q. Wang, B. Liu, X. Wang, S. Ran, L. Wang, D. Chen, and G. Shen, Morphology evolution of urchin-like NiCo₂O₄ nanostructures and their applications as pseudocapacitors and photoelectrochemical cells, *J. Mater. Chem.* **22**, 21647 (2012).
- [53] L. Hu, L. Wu, M. Liao, X. Hu, and X. Fang, Electrical transport properties of large, individual NiCo₂O₄ nanoplates, *Adv. Fun. Mat.* **22**, 998 (2012).
- [54] H. Zhao, S. Liu, R. Vellacheri, and Y. Lei, Recent advances in designing and fabricating self-supported nanoelectrodes for supercapacitors, *Adv. Sci.* **4**, 1700188 (2017).
- [55] A. Arico ograve, P. Bruce, B. Scrosati, J.-M. Tarascon, and W. van Schalkwijk, Nanostructured materials for advanced energy conversion and storage devices, *Nat. Mater.* **4**, 366 (2005).
- [56] G. Yu, L. Hu, N. Liu, H. E. Wang, M. Vosgueritchian, Y. Yang, Y. Cui, and Z. Bao, Enhancing the supercapacitor performance of Graphene/MnO₂ nanostructured electrodes by conductive wrapping, *Nano Lett.* **11**, 4438 (2011).
- [57] A. L. M. Reddy, S. R. Gowda, M. M. Shajumon, and P. M. Ajayan, Hybrid nanostructures for energy storage applications, *AdvanAdv. Mater* **24**, 5045 (2012).
- [58] L. Mai, X. Tian, X. Xu, L. Chang, and L. Xu, Nanowire electrodes for electrochemical energy storage devices, *Chem. Rev.* **114**, 11828 (2014).
- [59] L. Li *et al.*, One-dimension MnCo₂O₄ nanowire arrays for electrochemical energy storage, *Electrochim. Acta* **116**, 467 (2014).
- [60] D. Dubal, P. Gómez-Romero, B. Sankapal, and R. Holze, Nickel cobaltite as an emerging material for supercapacitors: An overview, *Nano Energy* **11** (2014).
- [61] G. Zhang and X. Lou, General solution growth of mesoporous nico₂o₄ nanosheets on various conductive substrates as high-performance electrodes for supercapacitors, *Adv. Mater.* **25**, 976 (2013).
- [62] X. Zheng, Y. Ye, Q. Yang, B. Geng, and X. Zhang, Hier-

- archical structures composed of $\text{MnCo}_2\text{O}_4@\text{MnO}_2$ core-shell nanowire arrays with enhanced supercapacitor properties, *Dalton Trans.* **45**, 572 (2016).
- [63] D. Cai *et al.*, Facile hydrothermal synthesis of hierarchical ultrathin mesoporous NiMoO_4 nanosheets for high performance supercapacitors, *Electrochim. Acta* **115**, 358 (2014).
- [64] I. Hussain, A. Ali, C. Lamiel, S. G. Mohamed, S. Sahoo, and J.-J. Shim, A 3D walking palm-like core-shell $\text{CoMoO}_4@\text{NiCo}_2\text{S}_4@\text{nickel}$ foam composite for high-performance supercapacitors, *Dalton Trans.* **48**, 3853 (2019).
- [65] J. Jiang, Y. Li, J. Liu, X. Huang, C. Yuan, and X. Lou, Recent advances in metal oxide-based electrode architecture design for electrochemical energy storage, *Adv. Mater.* **24**, 5166 (2012).
- [66] K. N. Hui, K. S. Hui, Z. Tang, V. Jadhav, and Q. X. Xia, Hierarchical chestnut-like MnCo_2O_4 nanoneedles grown on nickel foam as binder-free electrode for high energy density asymmetric supercapacitors, *J. Power Sources* **330**, 195 (2016).
- [67] X. Wang, H. Xia, J. Gao, B. Shi, Y. Fang, and M. Shao, Enhanced cycle performance of ultraflexible asymmetric supercapacitors based on a hierarchical $\text{MnO}_2@\text{NiMoO}_4$ core-shell nanostructure and porous carbon, *J. Mater. Chem. A* **4**, 18181 (2016).
- [68] Y. Zhang, J. Xu, Y. Zheng, Y. Zhang, X. hu, and T. Xu, $\text{NiCo}_2\text{S}_4@\text{NiMoO}_4$ core-shell heterostructure nanotube arrays grown on ni foam as a binder-free electrode displayed high electrochemical performance with high capacity, *Nanoscale Res. Lett.* **12**, 412 (2017).
- [69] J. Socratos *et al.*, Electronic structure of low-temperature solution-processed amorphous metal oxide semiconductors for thin-film transistor applications, *Adv. Funct. Mater.* **25**, 1873 (2015).
- [70] G. Zou, H. Li, Y. Zhang, K. Xiong, and Y. Qian, Solvothermal/hydrothermal route to semiconductor nanowires, *Nanotechnology* **17**, S313 (2006).
- [71] X.-h. Xia *et al.*, Freestanding Co_3O_4 nanowire array for high performance supercapacitors, *RSC Adv.* **2**, 1835 (2012).
- [72] R. Lee, The outlook for population growth, *Science* **333**, 569 (2011).
- [73] Z. Yao *et al.*, Homogeneous/inhomogeneous-structured dielectrics and their energy-storage performances, *Adv. Mater.* **29**, 1601727 (2017).
- [74] X. Y. Yu and X. W. (David) Lou, Mixed metal sulfides for electrochemical energy storage and conversion, *Adv. Energy Mater.* **8**, 1701592 (2018).
- [75] A. Burke and M. Miller, The power capability of ultracapacitors and lithium batteries for electric and hybrid vehicle applications, *J. Power Sources* **196**, 514 (2011).
- [76] F. Chen, X. Liu, Z. Zhang, N. Zhang, A. Pan, S. Liang, and R. Ma, Controllable fabrication of urchin-like Co_3O_4 hollow spheres for high-performance supercapacitors and lithium-ion batteries, *Dalton Trans.* **45**, 15155 (2016).
- [77] J. Lin *et al.*, Rational construction of nickel cobalt sulfide nanoflakes on CoO nanosheets with the help of carbon layer as the battery-like electrode for supercapacitors, *J. Power Sources* **362**, 64 (2017).
- [78] J. Lin *et al.*, Hierarchical $\text{CuCo}_2\text{O}_4@\text{NiMoO}_4$ core-shell hybrid arrays as a battery-like electrode for supercapacitors, *Inorg. Chem. Front.* **4**, 1575 (2017).
- [79] D. Cai *et al.*, Construction of unique NiCo_2O_4 nanowire@ CoMoO_4 nanoplate core/shell arrays on ni foam for high areal capacitance supercapacitors, *J. Mater. Chem. A* **2**, 4954 (2014).
- [80] Y. Liu, N. Fu, G. Zhang, M. Xu, W. Lu, L. Zhou, and H. Huang, Design of hierarchical ni–co@ni–co layered double hydroxide core-shell structured nanotube array for high-performance flexible all-solid-state battery-type supercapacitors, *Adv. Funct. Mater.* **27**, 1605307 (2017).
- [81] W. Xiao, J. S. Chen, C. Li, R. Xu, and X. Lou, Synthesis, characterization, and lithium storage capability of AMoO_4 ($A = \text{Ni}, \text{Co}$) nanorods, *Chem. Mater.* (2009).
- [82] Z. Zhang *et al.*, Facile synthesis of hierarchical $\text{CoMoO}_4@\text{NiMoO}_4$ core-shell nanosheet arrays on nickel foam as an advanced electrode for asymmetric supercapacitors, *J. Mater. Chem. A* **4**, 18578 (2016).
- [83] Y. Zhao, L. Hu, S. Zhao, and L. Wu, Preparation of $\text{MnCo}_2\text{O}_4@\text{Ni(OH)}_2$ core-shell flowers for asymmetric supercapacitor materials with ultrahigh specific capacitance, *Adv. Funct. Mater.* **26**, 4085 (2016).
- [84] K. Owusu *et al.*, Low-crystalline iron oxide hydroxide nanoparticle anode for high-performance supercapacitors, *Nat. Commun* **8**, 14264 (2017).
- [85] K. Xiao, L. Xia, G. Liu, S. Wang, L.-x. Ding, and H. Wang, Honeycomb-like nimoo₄ ultrathin nanosheet arrays for high-performance electrochemical energy storage, *J. Mater. Chem. A* **3**, 6128–6135 (2015).
- [86] M. Li, Y. Wang, H. Yang, and P. K. Chu, Hierarchical $\text{CoMoO}_4@\text{Co}_3\text{O}_4$ nanocomposites on an ordered macroporous electrode plate as a multi-dimensional electrode in high-performance supercapacitors, *J. Mater. Chem. A* **5**, 17312 (2017).
- [87] J. W. Long, B. Dunn, D. R. Rolison, and H. S. White, Three-dimensional battery architectures, *Chem. Rev.* **104**, 4463 (2004).
- [88] T. Nguyen, M. Boudard, L. Rapenne, O. Chaix-Pluchery, M. J. Carmezim, and M. F. Montemor, Structural evolution, magnetic properties and electrochemical response of mnco₂O₄ nanosheet films, *RSC Adv.* **5**, 27844 (2015).
- [89] W. Li, K. Xu, G. Song, X. Zhou, R. Zou, J. Yang, Z. Chen, and J. Hu, Facile synthesis of porous mnco₂O_{4.5} hierarchical architectures for high-rate supercapacitors, *CrystEngComm* **16**, 2335 (2014).
- [90] L. Li, F. He, S. Gai, S. Zhang, P. Gao, M. Zhang, Y. Chen, and P. Yang, Hollow structured and flower-like c@mnco₂O₄ composite for high electrochemical performance in a supercapacitor, *CrystEngComm* **16**, 9873 (2014).
- [91] Q. Yang and S.-Y. Lin, Rationally designed nanosheet-based comoo₄-nimoo₄ nanotubes for high-performance electrochemical electrodes, *RSC Adv.* **6**, 10520 (2016).
- [92] X. Wang, W. S. Liu, X. Lu, and P. S. Lee, Dodecyl sulfate-induced fast faradic process in nickel cobalt oxide-reduced graphite oxide composite material and its application for asymmetric supercapacitor device, *J. Mater. Chem.* **22**, 23114 (2012).
- [93] J. A.-A. Mehrez, K. A. Owusu, Q. Chen, L. Li, K. Hamwi, W. Luo, and L. Mai, Hierarchical mnco₂O₄@nimoo₄ as free-standing core-shell nanowire arrays with synergistic effect for enhanced supercapacitor performance, *Inorg. Chem. Front.* **6**, 857 (2019).
- [94] K. Xu *et al.*, Hierarchical mesoporous nico₂O₄@mno₂ core-shell nanowire arrays on nickel foam for aqueous asymmetric supercapacitors, *J. Mater. Chem. A* **2**, 4795 (2014).

- [95] X. Wang, H. Xia, J. Gao, B. Shi, Y. Fang, and M. Shao, Enhanced cycle performance of ultraflexible asymmetric supercapacitors based on a hierarchical $\text{mno}_2@\text{nimoo}_4$ core-shell nanostructure and porous carbon, *J. Mater. Chem. A* **4**, 18181 (2016).

Acknowledgements

The final end of this path required a lot of guidance and assistance from many people and I am extremely privileged to have got this all along the completion of my work. All that I have done is only due to such supervision and assistance and I would not forget to thank them.

First of all, I would like to express my deep respect to my supervisor, Prof Mai Liqiang for the opportunity to be under his supervision and to be part of his research group.

Also, I would like to acknowledge the assistance and guidance of Prof Zhou Liang and Dr Wen Luo completing my research and thesis on time. To my laboratory colleagues, especially Kwadwo Asare Owusu who walked with me step by step getting into the field of supercapacitors and to Lun Li and Qiang Chen who helped me during my course of study.

My final thanks go to my family.

Publications

[1] Jaafar Abdul-Aziz Mehrez, Kwadwo Asare Owusu, Qiang Chen, Lun Li, Khawla Hamwi, Wen Luo* and Liqiang Mai*, “Hierarchical MnCo₂O₄@NiMoO₄ as Free-Standing Core-Shell Nanowire Arrays with Synergistic Effect for Enhanced Supercapacitor Performance”, Inorganic Chemistry Frontiers, 2019. DOI: 10.1039/C8QI01420E.